

Parton-hadron-quantum-molecular dynamics: A novel microscopic n -body transport approach for heavy-ion collisions, dynamical cluster formation, and hypernuclei production

J. Aichelin,^{1,2} E. Bratkovskaya ,^{3,4} A. Le Fèvre,³ V. Kireyeu ,⁵ V. Kolesnikov ,⁵ Y. Leifels,³ V. Voronyuk,⁵ and G. Coci³

¹*SUBATECH, Université de Nantes, IMT Atlantique, IN2P3/CNRS 4 Rue Alfred Kastler, 44307 Nantes Cedex 3, France*

²*Frankfurt Institute for Advanced Studies, Ruth Moufang Straße 1, 60438 Frankfurt, Germany*

³*GSI Helmholtzzentrum für Schwerionenforschung GmbH, Planckstraße 1, 64291 Darmstadt, Germany*

⁴*Institut für Theoretische Physik, Johann Wolfgang Goethe-Universität, Max-von-Laue-Straße 1, 60438 Frankfurt am Main, Germany*

⁵*Joint Institute for Nuclear Research, Joliot-Curie 6, 141980 Dubna, Moscow Region, Russia*



(Received 8 July 2019; revised manuscript received 21 November 2019; accepted 13 March 2020; published 24 April 2020)

Cluster and hypernuclei production in heavy-ion collisions is presently under active experimental and theoretical investigation. Since clusters are weakly bound objects, their production is very sensitive to the dynamical evolution of the system and its interactions. The theoretical description of cluster formation is related to the n -body problem. Here we present the novel n -body dynamical transport approach PHQMD (parton-hadron-quantum-molecular dynamics) which is designed to provide a microscopic description of nuclear cluster and hypernucleus formation as well as of general particle production in heavy-ion reactions at relativistic energies. In contrast to the coalescence or statistical models, often used for the cluster formation, in PHQMD clusters are formed dynamically due to the interactions between baryons described on a basis of quantum molecular dynamics (QMD), which allows one to propagate the n -body Wigner density and n -body correlations in phase space, essential for the cluster formation. The clusters are identified by the MST (minimum spanning tree) procedure or the SACA (simulated annealing cluster algorithm) which finds the most bound configuration of nucleons and clusters. Collisions among hadrons as well as quark-gluon-plasma formation and parton dynamics in PHQMD are treated in the same way as in the established PHSD (parton-hadron-string dynamics) transport approach. In order to verify our approach with respect to the general dynamics, we present here the first PHQMD results for general “bulk” observables such as rapidity distributions and transverse mass spectra for hadrons (π , K , \bar{K} , p , \bar{p} , Λ , $\bar{\Lambda}$) from SIS (the GSI heavy ion synchrotron) to RHIC (BNL Relativistic Heavy Ion Collider) energies. We find a good description of the “bulk” dynamics which allows us to proceed with the results on cluster production, including hypernuclei.

DOI: [10.1103/PhysRevC.101.044905](https://doi.org/10.1103/PhysRevC.101.044905)

I. INTRODUCTION

There is a variety of evidence that a new state of matter, a quark-gluon plasma (QGP), has been created in experiments at the Relativistic Heavy Ion Collider (RHIC) at Brookhaven and at the Large Hadron Collider (LHC) at CERN [1]. The QGP has been predicted by lattice gauge calculations (lQCD) [2,3], in which the Lagrangian of quantum chromodynamics (QCD), describing strong-interacting matter, is calculated by computer. One of the unanswered questions is how the fraction of the matter in the QGP phase changes when lowering the beam energy and at what beam energy a QGP ceases to be created. At low beam energies, around a few A GeV, heavy-ion collisions (HICs) are successfully described by models which are based on hadronic degrees of freedom only. From experimental data at RHIC and LHC we know that at ultrarelativistic energies the baryon chemical potential in the midrapidity region is close to zero. By decreasing the beam energies one tests higher baryonic chemical potentials. However, for a large baryon chemical potential lQCD calculations cannot guide us because of the sign problem.

Phenomenological models, like those based on the Nambu–Jona-Lasinio Lagrangian, predict that the smooth transition (crossover) between the hadronic world and the QGP at vanishing baryon chemical potential [2,3] becomes a first-order phase transition for finite chemical potentials [4,5].

In order to study nuclear matter at high baryon densities, presently two accelerators are under construction: the Facility for Antiproton and Ion Research (FAIR) in Darmstadt and the Nuclotron-based Ion Collider fAcility (NICA) in Dubna. They will become operational in the coming years. Moreover, the presently running BES-II (Beam Energy Scan) at RHIC, which includes a fixed target program, provides experimental data in this energy regime. The scientific goal of all these experimental efforts is to study those observables which may carry information on the existence of the QGP and the nature of its phase transition to the hadronic world. These observables include the particle yields, rapidity and transverse momentum spectra of produced hadrons, their fluctuations and correlations with particular focus on the fluctuations of baryons, production of strange and multi-strange baryons, as well as cluster and hypernuclei production.

The study of cluster and hypernucleus production, which reflects the phase space density during the expansion phase, is of particular interest from the experimental as well as from the theoretical side. Experimentally, clusters have been observed at all energies: from low energies measured by the ALADIN [6,7], INDRA [8], FOPI [9], and HypHI [10] Collaborations to (ultra)relativistic energies measured by the NA49 [11], STAR [12,13], and ALICE [14–16] Collaborations.

The multiplicity of the produced clusters at midrapidity is related to the phase space distribution of baryons at their creation point, and therefore a change of the fluctuations—like that expected in the neighborhood of a first-order phase transition—will be directly reflected in the cluster multiplicity [17]. On the other hand, without identifying clusters, single-particle observables such as the baryon spectra cannot be correctly interpreted. This is especially important at low collision energies. For example, in central Au + Au collisions at 1.5A GeV only 65% of the total baryon charge is observed as protons, as measured by the FOPI Collaboration [9]; the rest is bound predominantly in light clusters. Composite clusters show different rapidity distributions, in-plane flows, and p_T spectra than free protons. Therefore, for the theoretical understanding of single-baryon spectra measured at those energies, one has to take into account the formation of clusters, otherwise predictions of observables are not precise, especially at low energies.

Among the clusters, hypernuclei which contain at least one hyperon (strange baryon) are the most interesting observables. The formation of hypernuclei in heavy-ion reactions has been a subject of many theoretical studies; cf. [17–24]. Recent experimental results [10,13,15] have shown that hypernuclei and antihypernuclei can be formed in heavy-ion collisions from SIS (the GSI heavy ion synchrotron) to LHC energies. Detailed theoretical calculations have identified two sources of hypernuclei in these reactions: In the overlap region of target and projectile, hyperons are produced in energetic first chance NN collisions. They (a) may migrate into the cold spectator matter, being there absorbed to form heavy hypernuclei, or (b) may stay in the participant region, which expands, and their interaction with the surrounding nucleons allows them to form light clusters and hence light hypernuclei. In view of their small binding energy and their hot environment this is like the creation of “ice in a fire.” Nevertheless, such hypernuclei have been found around midrapidity in RHIC and LHC experiments [10,15].

The two production mechanisms of hypernuclei may shed light on the theoretical understanding of the dynamical evolution of heavy-ion reactions which cannot be addressed by other probes. In particular, the formation of heavy projectile/target like hypernuclei elucidates the physics in the transition region between spectator and participant matter. Since hyperons are produced in the overlap region, multiplicity as well as rapidity distributions of hypernuclei formed in the target/projectile region depend crucially on the interactions of the hyperons with the hadronic matter, e.g., cross sections and potentials. On the other hand, midrapidity hypernuclei test the phase space distribution of baryons in the expanding participant matter, especially whether the phase space distributions of strange and nonstrange baryons are

similar and whether they are in thermal equilibrium. The present data [25,26] do not allow for a conclusive answer. The description of cluster and hypernuclei formation is a challenging theoretical task which requires (I) the microscopic dynamical description of the time evolution of heavy-ion collisions, and (II) the modeling of the mechanisms for the cluster formation.

The existing transport approaches are based on either (i) the quantum molecular dynamics (QMD) algorithms for the propagation of particles with mutual density dependent two-body potential interactions, e.g., QMD [26–29], IQMD [30], UrQMD [31,32], etc., or (ii) the mean-field based approaches such as different types of semiclassical (Vlasov) Boltzmann-Uehling-Uhlenbeck [(V)BUU] models, realized in terms of different numerical codes known as BUU [33–35], AMPT [36], HSD [37,38], PHSD [39], GiBUU [40], SMASH [41], etc. There are also models based on a cascade type propagation, such as the quark-gluon string model (QGS) [42].

The mean-field models reproduce well the single-particle observables; however, they are not suited for describing cluster formation since they propagate the single-particle distribution function (realized with the test particle method) in a mean-field potential calculated by averaging over many parallel ensembles. This approach smears out the initial n -body correlations as well as the dynamical correlations due to the interactions which develop during the whole time evolution of the system.

For the production of clusters, which are n -body correlations in phase space, one needs to calculate the time evolution of the n -body Wigner density [43]. Most of the presently available QMD approaches (QMD, IQMD) are limited to nonrelativistic energies. The only exception is the UrQMD approach, which has been used for study of deuteron and light nuclei production via coalescence [44].

Cluster formation has often been described either by a coalescence model [23,44] or statistical methods [22,45] assuming that during the heavy-ion reaction at least a subsystem achieves thermal equilibration. Both of these models have serious drawbacks. The most essential is that they are not able to address the question of how the clusters are formed and what we can learn from the cluster formation about the reaction dynamics.

In the coalescence model the multiplicity of clusters depends crucially on external parameters and the time t_C , when instantaneously the coalescence is calculated, as well as on the coalescence parameters. It neglects that energy and momentum conservation require the presence of another hadron during the cluster formation process and assumes that, after the clusters are identified at t_C , no further interactions of the cluster nucleons take place.

Such a sudden freeze-out is not in line with other observables like the resonance production. Decay products of resonances can interact with the surrounding medium; they are absorbed or rescattered, therefore the resonances cannot be identified anymore by the invariant mass method. Consequently, one observes experimentally a decrease of the multiplicity of resonances in comparison to the statistical model prediction. Such an effect is not properly treated within coalescence models.

There are some efforts made to improve the coalescence picture by extending it to the Wigner density approach. In this case the cluster formation at t_C is calculated by projecting the n -body Wigner density, which is propagated in the transport model, on the Wigner density of the ground states of the two-, three-, or four-body clusters. One uses a simple parametrization of the ground state wave function of the clusters which reproduces their rms (root-mean-square) radius. The Wigner density method allows one to predict the momentum distribution of these clusters and has been applied for the deuteron formation in heavy-ion reactions [23]. The drawbacks, however, remain that the origin of the cluster formation cannot be studied and that the dynamical cluster formation is reduced to a projection on the cluster Wigner density at a given time point t_C during the reaction.

Statistical fragmentation models are based on the strong assumption that a thermal equilibrium is obtained in heavy-ion reactions, at least in a limited rapidity interval. The single-particle spectra of protons and produced hadrons do not support such an assumption [46], at least not at the intermediate energies ($1A \leq E_{\text{beam}} \leq 30A$ GeV) on which we focus in this study. The statistical fragmentation model assumes, furthermore, that equilibrium is maintained during the expansion of the system up to very low densities where cluster formation sets in. The ingredients of the model—like the treatment of free and bound neutrons, the initial temperature, and the baryon chemical potential—are fitted to the experimental observations. The multiplicity of clusters observed with the high energy beams at RHIC and LHC experiments can be quantitatively described by statistical model calculations using the same parameters as for description of hadron multiplicities. The light cluster production can be described as well by a coalescence model [15]. Moreover, in Ref. [35] deuterons are produced and propagated by Green's function techniques. In Ref. [47] the deuteron production in Pb + Pb central collisions at LHC energies is assumed to be a final state interaction simulated by a two-step process $p + n \rightarrow d'$ and $d' + \pi \rightarrow d + \pi$ including a fictitious resonance d' .

In order to overcome these limitations we advance the novel parton-hadron-quantum-molecular dynamics (PHQMD) transport approach. The goal of this approach is to provide a dynamical description for the formation of light and heavy clusters and hypernuclei in relativistic heavy-ion collisions based on a microscopic origin, i.e., on the interaction between nucleons and hyperons which leads to the binding of clusters. Since clusters are weakly bound objects, they are very sensitive to the general dynamics of the system and to the interactions of the constituents, i.e., to the propagation and collisional interaction described by the kinetic equations of motion:

- (i) The PHQMD is based on the QMD dynamics for the propagation of the baryons, realized by density dependent two-body potential interactions [27,48,49], which allow (contrary to the mean-field approaches) one to propagate the n -body phase space correlations between baryons.
- (ii) In high energy heavy-ion collisions the dynamics is dominated by the multiparticle production at the early

stage with the formation of the QGP and partonic interactions. For the description of collisions and the QGP dynamics in PHQMD we adopt the collision integral of the parton-hadron-string dynamics approach (PHSD) [39,50–53], which was well tested in the reproduction of experimental data on “bulk” dynamics from SIS to LHC energies. Moreover, the original PHSD mean-field propagation (realized within the parallel ensemble method) for baryons is kept as an option, which will allow us to investigate the differences between the two approaches, i.e., the influence of QMD versus mean-field based propagation on “bulk” observables.

Thus, PHQMD provides a fully microscopic description of the time evolution of the system and the interactions between particles, on the hadronic and partonic levels. Due to that, in PHQMD the clusters are formed dynamically. This means that at the end of the heavy-ion reaction the same potential interaction, which is present during the whole time evolution, forms bound clusters of nucleons which are very distinct in phase space from other clusters and free nucleons. This differentiates our approach from coalescence models where at a given time point a coalescence radius in phase space is employed without considering whether the coalescing nucleons are still strongly interacting with nucleons which do not belong to the cluster.

These clusters can be identified by two methods: either by the minimum spanning tree (MST) procedure [27] or by a cluster finding algorithm based on the simulated annealing technique, the simulated annealing clusterization algorithm (SACA) [54,55]. Presently an extended version—fragment recognition in general application (FRIGA) [56]—is under development; it includes symmetry and pairing energy as well as hyperon-nucleon interactions.

The MST algorithm is based on spatial correlations and it is effective in finding the clusters at the end of the reaction. In order to identify the cluster formation already at early times of the reaction, when the collisions between the nucleons are still ongoing and the nuclear density is high, the SACA approach is used. It is based on the idea of Dorso and Randrup [57] that the most bound configuration of nuclei and nucleons evolves in time towards the final cluster distribution. The validity of this idea has been confirmed in numerical studies [58–60].

First results from the combined PHSD/SACA approach have been reported in [61]. There we applied SACA at some fixed time using the nucleon distribution from the PHSD at 11.45 GeV for semiperipheral Au + Au collisions. Moreover, the first attempt to identify hypernuclei with FRIGA has been reported in Refs. [56,61].

In this study we present the first results from the PHQMD approach. In order to validate the general dynamics in the PHQMD we start by presenting the results on “bulk” observables, covering the energy range from SIS to RHIC, and compare the PHQMD results with the PHSD results in order to identify the difference between the QMD and mean-field propagation of baryons, its influence on stopping of protons and, correspondingly, on the “chemistry” production and pressure redistribution in the interacting system, by looking at

rapidity distributions and transverse mass m_T or transverse momentum p_T spectra for hadrons (π , K , \bar{K} , p , \bar{p} , Λ , $\bar{\Lambda}$) from SIS to RHIC energies. Then we proceed with the first PHQMD results on dynamical cluster formation, including hypernuclei, based on the MST and SACA models. Furthermore, we verify our model the cluster production in comparison to the available experimental data at SIS energies, show the capacity of PHQMD to create clusters and hypernuclei at higher energies and make predictions for future FAIR and NICA experiments.

Our paper is organized as follows: We describe in Sec. II the basic ideas of the PHQMD model. In Sec. III we detail the algorithms (SACA and MST) which allow us to identify clusters in a dynamical model. In Sec. IV we present the results from the PHQMD for the “bulk” observables such as rapidity distributions and transverse mass or momentum spectra and compare them to available data from $E_{\text{beam}} = 1.5A$ GeV up to 21.3A TeV. Section V is devoted to the study of clusters. We confront our results with the existing data for heavy clusters and explore the formation of light clusters at midrapidity. Finally in Sec. VI we present our conclusions.

II. MODEL DESCRIPTION: THE PHQMD APPROACH

In this section we describe the basic ideas of the PHQMD approach. The PHQMD is an n -body microscopic transport approach which describes the time evolution of an interacting system by solving the kinetic equations of motion which contain (i) the propagation of degrees of freedom with their potential interaction as well as (ii) their scattering described by “collision integrals.” (iii) Moreover, the dynamically formed clusters are identified by the SACA and MST algorithms.

- (i) The propagation of baryons in PHQMD follows the quantum molecular dynamics (QMD) approach where baryons are described by Gaussian wave functions. In QMD the particles propagate under the influence of mutual two-body forces which are density dependent in order to approximate n -body forces ($n > 2$). The density is defined by the sum of the squares of the wave functions of all other nucleons. Both density independent and density dependent two-body forces are necessary to obtain a maximum of the binding energy at normal nuclear matter density. In such an approach “actio” is equal to “reactio” and, therefore, energy and momentum are strictly conserved. The strength of the interaction is chosen in a way that in infinite matter a given nuclear EoS is reproduced. The time evolution of the wave functions is determined according to a variational principle [62]. This approach conserves the phase space correlations in the system and does not suppress fluctuations as in mean-field based kinetic approaches. Since clusters are n -body correlations this approach is well suited to address the creation and time evolution of clusters.
- (ii) The PHQMD incorporates the collision integrals of the parton-hadron-string dynamics (PHSD) approach [39,50–53] which describes all interactions in the system—from primary hadron collisions to the

formation of the QGP in terms of strongly interacting quasiparticles (massive quarks and gluons); partonic interactions with further dynamical hadronization up to hadronic interactions during the final stage of the expansion. Moreover, the propagation of partonic degrees of freedom is adopted from the PHSD, too, and based on the Kadanoff-Baym equations [63] for the dynamics of strongly interacting systems [39,50,64].

- (iii) At the later stage of the reaction, after hadronization and resonance decays, the cluster recognition is performed by the SACA or MST algorithms which determine whether baryons are bound in clusters or not.

In the next subsections we will discuss the ideas of the PHQMD approach in more detail; however, for the readers who are familiar with the PHSD and QMD approaches we can summarize by saying that PHQMD combines the description of the QGP and hadronic interactions of the PHSD approach with the n -body dynamics and initial distributions of baryons from QMD. Additionally, cluster recognition algorithms MST and SACA, which are based on finding configurations with minimal binding (negative) energy calculated by the Weizsäcker mass formula, are applied.

A. Stages of the nucleus-nucleus collisions: The collision integral

Nucleus-nucleus collisions in the PHQMD (similarly to the PHSD) follow the following steps:

- (1) In the beginning of the nucleus-nucleus collision (an initialization of the nuclei as well as QMD propagation of nucleons will be discussed in the next section) two nuclei are approaching each other until they start to overlap such that individual nucleon-nucleon primary collisions take place. At relativistic energies the description of such primary collisions with multiparticle production is based on the Lund string model [65] which describes the energetic hadron-hadron collisions by the creation of excited color-singlet states, denoted “strings,” which are realized within the FRITIOF [65] and PYTHIA models [66] (cf. the HSD review [38] for the description of string dynamics in HICs). A string is composed of two string ends corresponding to the leading constituent quarks (antiquarks) of the colliding hadrons and a color flux tube (color-electric field) in between. As the string ends recede, virtual $q\bar{q}$ or $qq\bar{q}\bar{q}$ pairs are produced in the uniform color field by a tunneling process (described by the Schwinger formula [67]), causing the breaking of the string. The produced quarks and antiquarks recombine with neighboring partons into “prehadronic” states which will approach hadronic quantum states (mesons or baryon-antibaryon pairs) after a formation time $\tau_f \approx 0.8$ fm/ c (in the rest frame of the string). In the calculational frame of the heavy-ion reaction (which is chosen to be the initial NN center-of-mass frame) the formation time then is $t_F = \tau_f \gamma$, where $\gamma = 1/\sqrt{1-v^2}$ and v is the velocity of the particle in the calculational frame.

In the string decay, the flavor of the produced quarks is determined via the Schwinger formula [66,67], which defines the production probability of massive $s\bar{s}$ pairs with respect to light flavor production ($u\bar{u}$, $d\bar{d}$) pairs:

$$\frac{P(s\bar{s})}{P(u\bar{u})} = \frac{P(s\bar{s})}{P(d\bar{d})} = \gamma_s = \exp\left(-\pi \frac{m_s^2 - m_{u,d}^2}{2\kappa}\right), \quad (1)$$

with $\kappa \approx 0.176 \text{ GeV}^2$ denoting the string tension and $m_{u,d,s}$ the constituent quark masses for strange and light quarks. For the constituent quark masses $m_u \approx 0.35 \text{ GeV}$ and $m_s \approx 0.5 \text{ GeV}$ are adopted in the vacuum; the production of strange quarks thus is suppressed by a factor of $\gamma_s \approx 0.3$ with respect to the light quarks, which is the default setting in the FRITIOF routines. We note that in Refs. [68,69] the PHSD has been extended to include the chiral symmetry restoration (CSR) effect in the string decay by changing of constituent quark masses due to the dropping of the scalar quark condensate in a hadronic environment of a finite baryon and meson density. After string decay the “leading hadrons,” which originate from the string ends, can reinteract with hadrons almost instantly with reduced cross sections (according to the constituent quark number) [38].

- (2) If the local energy density in the cell is above the critical value of $\epsilon_c \approx 0.5 \text{ GeV/fm}^3$, the “deconfinement” (i.e., a transition of hadronic to partonic degrees of freedom) is implemented by dissolving the “prehadrons” (the string decay products which are in this cell) into the massive colored quarks/antiquarks and mean-field energy, keeping “leading hadrons” out of dissolution (cf. Refs. [39,51] for the details). This procedure allows one to keep the microscopic description of changing degrees of freedom by conserving the energy-momentum, charge, flavor, etc.

In PHQMD (as well as in PHSD) the partonic (or the QGP phase) is based on the dynamical quasiparticle model (DQPM) [70,71] which describes the properties of QCD (in equilibrium) in terms of resummed single-particle Green’s functions. Instead of massless partons of pQCD, in PHSD the gluons and quarks are massive strongly interacting quasi particles, which reflects the nonperturbative nature of the strong interaction. The properties of off-shell quasiparticles are described by spectral functions (imaginary parts of the complex propagators) with temperature dependent masses and widths. The widths and pole positions of the spectral functions are defined by the real and imaginary parts of the parton self-energies and the effective coupling strength which is fixed by adjusting IQCD results for the entropy density [72–74] (using in total three parameters). The details of the DQPM model, adopted in the PHQMD, can be found in Appendix A.

- (3) Within the QGP phase, the partons (quarks, antiquarks, and gluons) scatter and propagate in a self-generated scalar mean-field potential [51]. On the partonic side the elastic and inelastic interactions $qq \leftrightarrow qq$, $q\bar{q} \leftrightarrow$

$q\bar{q}$, $gg \leftrightarrow gg$, $gg \leftrightarrow g$, $q\bar{q} \leftrightarrow g$ are included, exploiting “detailed balance” with temperature dependent cross sections (as in the PHSD 4.0) (cf. [53,75]). The propagation of off-shell partons in PHQMD (as well as in PHSD) is fully determined by the Cassing-Juchem off-shell transport equations based on the Kadanoff-Baym equations (cf. the review [50]).

- (4) The expansion of the system leads to a decrease of the local energy density and, once the local energy density becomes close to or lower than ϵ_c , the massive colored off-shell quarks and antiquarks hadronize to colorless off-shell mesons and baryons. The hadronization process is defined by covariant transition rates (see Appendix B) and fulfills the energy-momentum and quantum number conservation in each event [51].
- (5) In the hadronic “corona” (i.e. the region with low energy density) as well as in the late hadronic phase after hadronization, or even the whole dynamics at low bombarding energies (without the formation of the QGP), the hadrons are interacting and propagating. The hadronic degrees of freedom in the PHQMD are the baryon octet and decuplet, the 0^- and 1^- meson nonets, and higher resonances. The hadronic interactions include elastic and inelastic collisions between baryons, mesons, and resonances (including the backward reactions through detailed balance) in line with the HSD approach [37,38]. We note that in the PHQMD (as well as in the PHSD) the multimeson fusion reactions to baryon-antibaryon pairs and backward reactions (n mesons $\leftrightarrow B + \bar{B}$) are included, too [76,77]. The PHQMD (as well as PHSD) incorporates also the in-medium effects, i.e., the changes of hadronic properties in the dense and hot environment, such as a collisional broadening of spectral functions of vector mesons (ρ , ω , ϕ , a_1) [78], strange mesons K , \bar{K} [79], and strange vector mesons K^* , \bar{K}^* [80]. The propagation of the off-shell mesonic states is described also by the Cassing off-shell transport equations [50,79]. Contrary to the PHSD, the propagation of baryonic states in the PHQMD follow the QMD equations (see Sec. II C).

In the PHQMD approach the full evolution of a relativistic heavy-ion collision—from the initial hard NN collisions out of equilibrium, to the formation of a partonic state, the hadronisation as well as final interactions of the resulting hadronic particles—is described on the same footing.

B. Initialization of the nuclei

As mentioned above, we adopt the parallel ensemble method for the PHQMD approach for both dynamical options: QMD (where the parallel ensembles are independent) and mean field (MF) used in the PHSD. In the MF (i.e., PHSD) mode the initialization in coordinate space is realized by pointlike test particles, randomly distributed according to the Wood-Saxon density distribution and in momentum space according to the local Thomas-Fermi distribution in the rest frame of the nucleus.

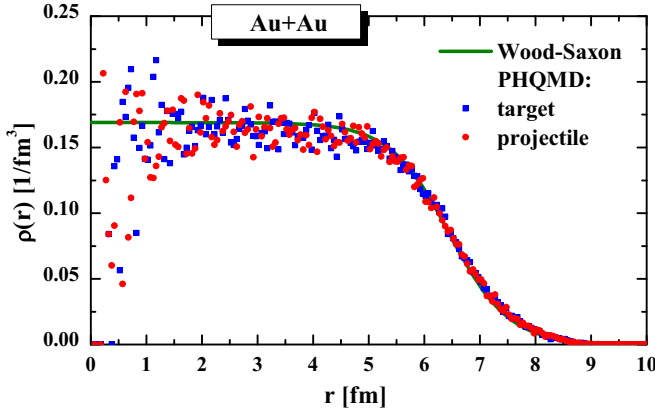


FIG. 1. The averaged (over 250 events) density distribution of target (blue squares) and projectile (red dots) nucleons in Au + Au collisions obtained from the QMD initialization in comparison to the Wood-Saxon distribution, Eq. (4) (solid line).

In the QMD mode we use the single-particle Wigner density of the nucleon i , which is given by

$$f(\mathbf{r}_i, \mathbf{p}_i, \mathbf{r}_{i0}, \mathbf{p}_{i0}, t) = \frac{1}{\pi^3 \hbar^3} e^{-\frac{2}{L}[\mathbf{r}_i - \mathbf{r}_{i0}(t)]^2} e^{-\frac{L}{2\hbar^2}[\mathbf{p}_i - \mathbf{p}_{i0}(t)]^2}, \quad (2)$$

where the Gaussian width L is taken as $L = 2.16 \text{ fm}^2$. We will use the $\hbar = c = 1$ convention for further consideration. The corresponding single-particle density is obtained by an integration of the single-particle Wigner density over the momentum of nucleon i :

$$\begin{aligned} \rho_{sp}(\mathbf{r}_i, \mathbf{r}_{i0}, t) &= \int d\mathbf{p}_i f(\mathbf{r}_i, \mathbf{p}_i, \mathbf{r}_{i0}, \mathbf{p}_{i0}, t) \\ &= \left(\frac{2}{\pi L}\right)^{3/2} e^{-\frac{2}{L}[\mathbf{r}_i - \mathbf{r}_{i0}(t)]^2}. \end{aligned} \quad (3)$$

The total one-body Wigner density is the sum of the Wigner densities of all nucleons. To initialize the nuclei we choose randomly the position of nucleons $\mathbf{r}_{i0}(t = 0)$ according to the Wood-Saxon density distribution. We take care that the distribution is smooth by requiring a minimal phase space distance between the nucleons. Figure 1 shows the nucleon density distribution (averaged over 250 QMD events) of target and projectile nucleons in Au + Au collisions in comparison to the Wood-Saxon distribution

$$\rho^{WS}(r) = \frac{\rho_0}{1 + e^{\frac{r-R_A}{a}}}, \quad (4)$$

where $R_A = r_0 A^{1/3}$ is the radius of nuclei with mass number A with $r_0 = 1.125 \text{ fm}$, $\rho_0 = 0.1695 \text{ fm}^{-2}$, $a = 0.535 \text{ fm}$.

To initialize the nuclei in momentum space, we chose randomly the momenta of nucleons, $\mathbf{p}_{i0}(t = 0)$, according to the Thomas-Fermi distribution with the additional requirement that the nucleons are bound:

$$0 \leq \sqrt{m^2 + \mathbf{p}_{i0}^2(t = 0)} - m \leq -\langle V(\mathbf{r}_{i0}) \rangle, \quad (5)$$

where m is the mass of a nucleon. Here the expectation value of the potential energy $\langle V(\mathbf{r}_{i0}) \rangle$ (which we discuss in the next subsection) is negative. This procedure gives a lower momentum to those nucleons which are located close to the

surface because there the density is lower. Finally we take care that $\sum_i \mathbf{p}_{i0}(t = 0) = 0$ by adding a common momentum to all nucleons.

With such determined momenta and positions we calculate the average binding energy of the nucleons and compare the result with the Bethe-Weizsäcker mass formula. It turns out that we underestimate slightly the average binding energy independently of the size of the nucleus. To obtain the right binding energy we multiply the momenta of all nucleons by a common factor (close to 1). This factor depends on the value of L . Before the nuclei collide, target and projectile nucleons are boosted into the nucleus-nucleus center-of-mass frame and get Lorentz contracted.

C. QMD propagation

The propagation of the Wigner density is determined by a variational principle [62], which has been developed for the time dependent Hartree-Fock approach:

$$\delta \int_{t_1}^{t_2} dt \langle \psi(t) | i \frac{d}{dt} - H | \psi(t) \rangle = 0. \quad (6)$$

In our approach we assume that the n -body Wigner density is the direct product of the single-particle Wigner densities. There are also QMD versions which use a Slater determinant, FMD [62] and AMD [81], but due to the difficulty of formulating collision terms these approaches have only been applied to low energy heavy-ion collisions. Assuming that the wave functions have a Gaussian form and that the width of the wave function is time independent, one obtains for the time evolution of the centroids of the Gaussian single-particle wave functions two equations which resemble the equation of motion of a classical particle with the phase space coordinates $\mathbf{r}_{i0}, \mathbf{p}_{i0}$ [27]. The difference is that here the expectation value of the quantal Hamiltonian is used and not a classical Hamiltonian:

$$\dot{r}_{i0} = \frac{\partial \langle H \rangle}{\partial p_{i0}}, \quad \dot{p}_{i0} = -\frac{\partial \langle H \rangle}{\partial r_{i0}}. \quad (7)$$

These time evolution equations are specific for Gaussian wave functions. For other choices of wave functions the time evolution equations would be different. The Hamiltonian of the nucleus is the sum of the Hamiltonians of the nucleons, composed of kinetic and two-body potential energies:

$$H = \sum_i H_i = \sum_i (T_i + V_i) = \sum_i \left(T_i + \sum_{j \neq i} V_{i,j} \right). \quad (8)$$

The interaction between the nucleons has two parts, a local Skyrme type interaction and a Coulomb interaction:

$$\begin{aligned} V_{i,j} &= V(\mathbf{r}_i, \mathbf{r}_j, \mathbf{r}_{i0}, \mathbf{r}_{j0}, t) = V_{\text{Skyrme}} + V_{\text{Coul}} \\ &= \frac{1}{2} t_1 \delta(\mathbf{r}_i - \mathbf{r}_j) + \frac{1}{\gamma + 1} t_2 \delta(\mathbf{r}_i - \mathbf{r}_j) \rho^{\gamma-1} \\ &\quad \times (\mathbf{r}_i, \mathbf{r}_j, \mathbf{r}_{i0}, \mathbf{r}_{j0}, t) + \frac{1}{2} \frac{Z_i Z_j e^2}{|\mathbf{r}_i - \mathbf{r}_j|}, \end{aligned} \quad (9)$$

with the density $\rho(\mathbf{r}_i, \mathbf{r}_j, \mathbf{r}_{i0}, \mathbf{r}_{j0}, t)$ defined as

$$\begin{aligned} \rho(\mathbf{r}_i, \mathbf{r}_j, \mathbf{r}_{i0}, \mathbf{r}_{j0}, t) &= C \frac{1}{2} \left[\sum_{j, i \neq j} \left(\frac{1}{\pi L} \right)^{3/2} e^{-\frac{1}{L}[\mathbf{r}_i - \mathbf{r}_j - \mathbf{r}_{i0}(t) + \mathbf{r}_{j0}(t)]^2} \right. \\ &\quad \left. + \sum_{i, i \neq j} \left(\frac{1}{\pi L} \right)^{3/2} e^{-\frac{1}{L}[\mathbf{r}_i - \mathbf{r}_j - \mathbf{r}_{i0}(t) + \mathbf{r}_{j0}(t)]^2} \right]. \end{aligned} \quad (10)$$

where C is a correction factor explained below.

We define the ‘‘interaction’’ density $\rho_{int}(\mathbf{r}_{i0}, t)$, which for the nonrelativistic case can be written as

$$\rho_{int}(\mathbf{r}_{i0}, t) = C \sum_{j, j \neq i} \left(\frac{1}{\pi L} \right)^{3/2} e^{-\frac{1}{L}[\mathbf{r}_{i0}(t) - \mathbf{r}_{j0}(t)]^2}. \quad (11)$$

The interaction density has twice the width of the particle density, Eq. (3), and is obtained by calculating the expectation value of the local Skyrme potential which is $\propto \delta(\mathbf{r}_i - \mathbf{r}_j)$. The correction factor C in Eq. (10) depends on L . It is introduced because nuclear densities are calculated differently in mean-field approaches—for which the Skyrme parametrization has been developed—and QMD approaches. In mean-field transport or hydrodynamical approaches the density which enters the density dependent two-body interaction is obtained by summing over all particles in the system: $\rho_{int}^{MF}(\mathbf{r}_{i0}, t) = \sum_j \dots$. In QMD type approaches we have to exclude self-interactions and therefore the density which enters the density dependent interaction is the sum over all nucleons with the exception of that nucleon on which this density dependent potential acts: $\rho_{int}(\mathbf{r}_{i0}, t) = \sum_{j \neq i} \dots$.

The two densities differ by $(\frac{1}{\pi L})^{3/2}$. To compensate for the lower density in the QMD type approaches compared to the mean-field approaches, we introduce the correction factor C which is adjusted numerically to achieve equality of the two densities. With this correction factor we can use the Skyrme potentials also for the QMD approach.

The expectation value of the potential energy V_i , $\langle V_i \rangle = \langle V(\mathbf{r}_{i0}, t) \rangle$, of the nucleon i is given by

$$\begin{aligned} \langle V(\mathbf{r}_{i0}, t) \rangle &= \sum_{j, j \neq i} \int d^3 r_i d^3 r_j d^3 p_i d^3 p_j V(\mathbf{r}_i, \mathbf{r}_j, \mathbf{r}_{i0}, \mathbf{r}_{j0}) \\ &\quad \times f(\mathbf{r}_i, \mathbf{p}_i, \mathbf{r}_{i0}, \mathbf{p}_{i0}, t) f(\mathbf{r}_j, \mathbf{p}_j, \mathbf{r}_{j0}, \mathbf{p}_{j0}, t). \end{aligned} \quad (12)$$

Numerical tests have shown that the time evolution of the system does not change if we replace $\frac{1}{2}[\rho_{int}(\mathbf{r}_{i0}, t) + \rho_{int}(\mathbf{r}_{j0}, t)]$ by $\rho_{int}(\mathbf{r}_{i0}, t)$ or by $\rho_{int}(\mathbf{r}_{j0}, t)$. For the Skyrme potential we can therefore use the analytical form

$$\langle V_{\text{Skyrme}}(\mathbf{r}_{i0}, t) \rangle = \alpha \left(\frac{\rho_{int}(\mathbf{r}_{i0}, t)}{\rho_0} \right) + \beta \left(\frac{\rho_{int}(\mathbf{r}_{i0}, t)}{\rho_0} \right)^\gamma. \quad (13)$$

The expectation value of the Coulomb interaction can also be calculated analytically.

TABLE I. Parameter sets for the nuclear equation of state used in the PHQMD model.

	α (MeV)	β (MeV)	γ	K (MeV)
S	-390	320	1.14	200
H	-130	59	2.09	380

The expectation value of the Hamiltonian which enters in Eq. (7) is finally given by

$$\begin{aligned} \langle H \rangle &= \langle T \rangle + \langle V \rangle \\ &= \sum_i (\sqrt{p_{i0}^2 + m^2} - m) + \sum_i \langle V_{\text{Skyrme}}(\mathbf{r}_{i0}, t) \rangle. \end{aligned} \quad (14)$$

The nuclear equation of state (EoS) describes the variation of the energy $E(T = 0, \rho/\rho_0)$ when changing the nuclear density in infinite matter to values different from the saturation density ρ_0 for zero temperature. In infinite matter the density is position independent and we can use Eq. (13) to connect our Hamiltonian with nuclear matter properties, because for a given value of γ the parameters t_1, t_2 in Eq. (9) are uniquely related to the coefficients α, β of the EoS, Eq. (13). Values of these parameters for the different model choices can be found in Table I.

Two of the three parameters of the Skyrme potential can be fixed by the condition that the energy per nucleon has a minimum of $\frac{E}{A}(\rho_0) = -16$ MeV at ρ_0 .

The third equation is historically provided by fixing the compression modulus K of nuclear matter, the inverse of the compressibility $\chi = \frac{1}{V} \frac{dV}{dP}$, which corresponds to the curvature of the Skyrme energy at $\rho = \rho_0$ (for $T = 0$) that is also given in Table I:

$$K = -V \frac{dP}{dV} = 9\rho^2 \frac{\partial^2 [E/A(\rho)]}{(\partial \rho)^2} \Big|_{\rho=\rho_0}. \quad (15)$$

Here P is the pressure in the system of volume V . An equation of state with a rather low value of the compression modulus K yields a weak repulsion against the compression of nuclear matter and thus describes ‘‘soft’’ matter (denoted by ‘‘S’’). A high value of K causes a strong repulsion of nuclear matter under compression (called a hard EoS, ‘‘H’’). The hard and soft equations of state used in this study are illustrated in Fig. 2.

We stress again that for the present study we use a ‘‘static’’ form of Skyrme potential which depends only on the local density according to Eq. (12). A momentum dependent Skyrme interaction is more realistic. This will be the subject of future studies. Many observables show for a soft momentum dependent interaction and a static hard interaction quite similar results [28]. We also note that in the PHQMD we propagate nonstrange baryon resonances (such as Δ 's) in the same manner as nucleons, assuming the same potential interaction as the nucleon-nucleon one, while for strange baryon resonances (such as Λ 's, Σ 's) we assume 2/3 of the nucleon-nucleon potential.

The influence of the nucleon potential and hence of the EoS on hadronic observables as well as on the cluster formation in heavy-ion collisions is well established at low energies (cf., e.g., [46]) where the nonrelativistic Hamiltonian formulation

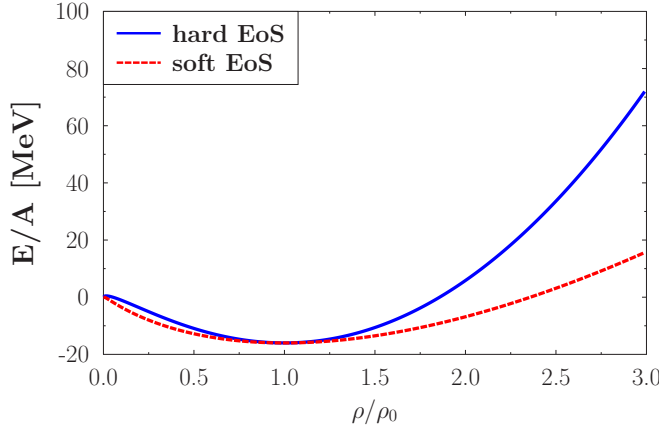


FIG. 2. The energy per nucleon for the two EoS: hard (solid blue line) and soft (dotted red line).

of QMD (presented in this section) is applicable. With increasing bombarding energies a relativistic dynamics becomes more important. The relativistic formulation of molecular dynamics has been developed in Ref. [48]; however, the numerical realization of this method for realistic heavy-ion calculations is still not achievable with present computer power since it takes about two orders of magnitude longer time to simulate the reaction due to the inversion of high dimensional matrices. Therefore, we are facing the problem of how to extend the nonrelativistic QMD approach to the high energy collisions considered in this study, within a framework which can be numerically realized.

In order to extend our approach for relativistic energies, we introduce the modified single-particle Wigner density \tilde{f} of the the nucleon i :

$$\begin{aligned} \tilde{f}(\mathbf{r}_i, \mathbf{p}_i, \mathbf{r}_{i0}, \mathbf{p}_{i0}, t) &= \frac{1}{\pi^3} e^{-\frac{2}{L}[\mathbf{r}_i^T(t) - \mathbf{r}_{i0}^T(t)]^2} e^{-\frac{2\gamma_{cm}}{L}[\mathbf{r}_i^L(t) - \mathbf{r}_{i0}^L(t)]^2} \\ &\times e^{-\frac{1}{2}[\mathbf{p}_i^T(t) - \mathbf{p}_{i0}^T(t)]^2} e^{-\frac{L}{2\gamma_{cm}}[\mathbf{p}_i^L(t) - \mathbf{p}_{i0}^L(t)]^2}, \end{aligned} \quad (16)$$

which accounts for the Lorentz contraction of the nucleus in the beam z direction, in coordinate and momentum space, by inclusion of $\gamma_{cm} = 1/\sqrt{1 - v_{cm}^2}$, where v_{cm} is a velocity of the bombarding nucleon in the initial NN center-of-mass system. Accordingly, the interaction density (11) becomes

$$\begin{aligned} \tilde{\rho}_{int}(\mathbf{r}_{i0}, t) &\rightarrow C \sum_j \left(\frac{1}{\pi L} \right)^{3/2} \gamma_{cm} e^{-\frac{1}{L}[\mathbf{r}_{i0}^T(t) - \mathbf{r}_{j0}^T(t)]^2} \\ &\times e^{-\frac{\gamma_{cm}}{L}[\mathbf{r}_{i0}^L(t) - \mathbf{r}_{j0}^L(t)]^2}. \end{aligned} \quad (17)$$

With these modifications we obtain

$$\langle \tilde{H} \rangle = \sum_i \left(\sqrt{p_{i0}^2 + m^2} - m \right) + \sum_i \langle \tilde{V}_{\text{Skyrme}}(\mathbf{r}_{i0}, t) \rangle \quad (18)$$

with

$$\langle \tilde{V}_{\text{Skyrme}}(\mathbf{r}_{i0}, t) \rangle = \alpha \left(\frac{\tilde{\rho}_{int}(\mathbf{r}_{i0}, t)}{\rho_0} \right) + \beta \left(\frac{\tilde{\rho}_{int}(\mathbf{r}_{i0}, t)}{\rho_0} \right)^\gamma, \quad (19)$$

with the time evolution equations (7).

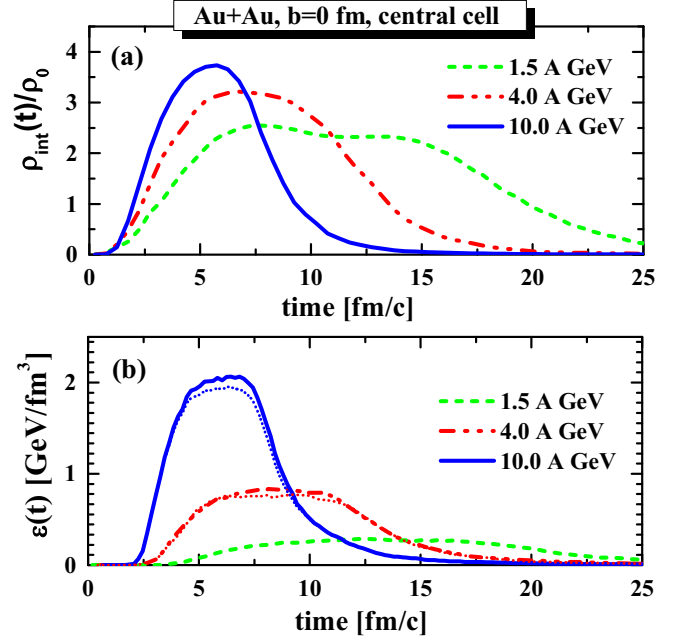


FIG. 3. Time evolution of the interaction density, scaled to the normal nuclear density $\rho_0 = 0.168 \text{ fm}^{-3}$ (upper plot), and the energy density (lower plot) in the central cell of volume $(27/\gamma_{cm}) \text{ fm}^3$ of Au + Au collisions at $E_{\text{beam}} = 1.5\text{A GeV}$ (dashed green lines), 4.0A GeV (dash-dotted red lines), and 10.0A GeV (solid blue lines), averaged over 200 events. The dotted red and blue lines in the lower plot show the hadronic contribution to the energy density for the corresponding beam energies of 4.0A GeV and 10.0A GeV .

To verify the applicability of our ansatz for the relativistic extension of the interaction density, Eq. (16), we have analyzed the time evolution of the interaction density. In the upper part of Fig. 3 we show the time evolution of the interaction density, scaled to the normal nuclear density $\rho_0 = 0.168 \text{ fm}^{-3}$, of all baryons in the central cell of a volume $(27/\gamma_{cm}) \text{ fm}^3$ of Au + Au collisions at $E_{\text{beam}} = 1.5\text{A GeV}$ (dashed green lines), 4.0A GeV (dash-dotted red lines), and 10.0A GeV (solid blue lines), averaged over 200 events. One can see that at 4A and 10A GeV in the central cell a maximal density ρ_{int} of 3–3.5 ρ_0 can be reached during the overlap of the nuclei. The lower part of Fig. 3 shows the time evolution of the local energy density ϵ of all interacting particles (hadrons and partons), in the central cell (with color coding as for the upper plot). The dotted red and blue lines in the lower plot show the hadronic contribution to the energy density for the corresponding beam energies of 4.0A GeV and 10.0A GeV . One can see that at the low bombarding energy of 1.5A GeV the energy density in the center of the fireball is rather small and always below the critical one. In spite of the energy density increasing with bombarding energy, the matter is still hadron dominated at 4A and 10A GeV, and the QGP is formed only in small droplets, i.e., the fraction of the QGP in the total energy balance of the system is still very small at such energies and increases slowly with growing bombarding energy (cf. Fig. 4 in Ref. [82]). This is related to the fact that in PHQMD (as in PHSD) the leading hadrons—the fastest ends of the decaying

strings, which are rather short (i.e., have little energy) at low energies—are not dissolved (as explained in Sec. II A) to partons and keep their hadronic identity. However, with increasing bombarding energy the fraction of partonic degrees of freedom grows and at RHIC energies it dominates the hadronic one in the central cells. Shortly after hadronization, the hadronic collisions are still frequent and the momentum transfer due to collisions is large relative to the momentum transfer due to the potential interactions between hadrons. Only later during the expansion, when the mean-free path becomes large, does the momentum change due to the potential interaction dominate again. However, the potential interaction in the QMD propagation is relevant for the spectators and baryons in the relatively cold “corona” during the whole time evolution of the system.

Summarizing, at higher beam energies the potential interactions are important in the following cases:

- (i) For midrapidity baryons during the final hadronic phase of the expanding system when the mean free path of hadrons is long, which might lead to the formation of light clusters. In this expanding region the inverse slope parameters of the transverse energy spectra of the baryons are of the order of 100 MeV and therefore for all baryons we are in an approximately nonrelativistic regime.
- (ii) For spectator baryons (nucleons) at all energies and during the whole time evolution. There the Pauli principle does not allow for collisions of nucleons because the phase space of the outgoing channel is already occupied by other nucleons. Thus, the rapidity distribution of spectators changes only little during the reaction and they are finally the source of heavy clusters. Here the relative momentum between two nucleons is of the order of the Fermi momentum and therefore we can as well apply nonrelativistic kinematics.

D. Pauli blocking

The collisions in the overlapping zone of projectile and target are rather energetic and therefore the phase space of their final state is empty. This is not the case for collisions in the spectator matter or for participants which enter the spectator matter. There, the final phase space is occupied in many cases, thus the collision is Pauli blocked. The evaluation of the Pauli blocking is a nontrivial task in QMD calculations due to the problem of defining a surface of the nucleus. For nucleons in the center of the reaction zone, where the phase space occupation is close to unity, one can calculate the phase space occupation and apply a Monte Carlo approach to define whether the collision is allowed or not. At the surface it is more difficult because the initial nucleus has there a low phase space density. For this case a special algorithm has been developed which blocks also the collisions close to the surface effectively. For a single Au nucleus, initialized with our initialization routine, where all collisions should be blocked, we obtain a blocking rate of 96%. More details of the

quantum molecular dynamics (QMD) approach can be found in [27,30,46].

III. CLUSTER FORMATION: SACA AND MST

A. Algorithms for cluster formation

Since the transport models propagate nucleons, one needs to define a consistent theoretical approach to build clusters out of these nucleons. In our approach clusters are formed by the same nucleon-nucleon interactions which rule the time evolution of the system in the course of the heavy-ion collision. We call this *dynamical* cluster formation in contradistinction to models where fragments are created instantaneously at a given time as in coalescence models. As discussed in the Introduction, we employ here the following two procedures for the dynamical cluster identification:

- (1) MST (minimum spanning tree) [27]. In this approach only the coordinate space information is used to define clusters. Therefore, this method can identify clusters only when free nucleons and groups of nucleons, called clusters, are well separated in coordinate space at the end of the reaction. Then two nucleons are considered as part of a cluster if their distance is less than $r_0 = 2.5$ fm. Nucleons which are connected by this condition form a cluster. Nucleons with a large relative momentum are no longer close to each other at late times. Consequently, additional cuts in momentum space change the cluster distribution only little.
- (2) SACA (simulated annealing clusterization algorithm) [54,55]. To overcome the limitation that clusters can only be identified at the end of the reaction we have developed the simulated annealing cluster Algorithm (SACA) approach [54,55]. It is based on the idea of Dorso and Randrup [57] that the most bound configuration of nucleons and clusters, identified during the reaction, has a large overlap with the final distribution of clusters and free nucleons. This allows one to study the clusterization pattern early, shortly after the passing time (the time the two nuclei need to pass each other) when the different final clusters still overlap in coordinate space. Dorso and Randrup could demonstrate this for small systems and Puri *et al.* [54,55] found out that it is also true for large systems. To obtain the most bound configuration, one calculates for each possible configuration of clusters and free nucleons the total binding energy: the sum of the binding energies of all clusters. The potential interaction between clusters is neglected as well as that between free nucleons and clusters. The binding energy is calculated using the Skyrme interaction, Eq. (19). This procedure allows one to identify the clusters early during the reaction and allows therefore for the study of the origin of physical processes which involve clusters. To determine the most bound configuration, the simulated annealing technique has been employed [54,55], a probabilistic numerical method (realized via a Metropolis algorithm) for finding the global minimum of a given function under constraints.

For very late times the differences between a fully quantal and our semiclassical approach may influence the cluster distribution because the ground state of a cluster as a quantum system of fermions has to respect a minimal average kinetic energy of the nucleons (the Fermi energy if the nucleons are confined in a sphere) whereas that of our semiclassical approach does not have to obey this condition. Therefore, nucleons may still be emitted even if in the corresponding quantum system this is not possible anymore. It takes, however, quite long, considerably more than $100 \text{ fm}/c$, until one of the cluster nucleons gains so much kinetic energy that it can overcome the potential barrier.

None of these approaches to determine clusters influences the time evolution of the heavy-ion reaction. The underlying PHQMD approach propagates in the QMD mode only baryons, but not clusters. If applied at different times during a heavy-ion reaction, the SACA approach allows one to study the time evolution of cluster formation. It has been shown that for large times SACA and MST yield very similar results [54,55] and that the results agree well with the experimental findings for clusters with $Z \geq 3$ [83].

We note that the clusterization algorithms (SACA and MST) find clusters in the rest frame of target/projectile spectators while the heavy-ion dynamics is realized in the initial NN center-of-mass system in which spectators are squeezed due to the Lorentz contraction of initial nuclei at relativistic energies; cf. Eq. (17). In order to obtain the right kinematical “input” for finding the cluster in the spectator regions, we apply the inverse Lorentz transformation with γ_{cm} containing the velocity between the NN center of mass and the respective rest system at target/projectile region. This approximation is justified even at high beam energies since with increasing γ_{cm} the passing time of the heavy nuclei decreases as compared to R/v_{Fermi} (where R is the radius of the nucleus and v_{Fermi} is the Fermi velocity). Thus, the spectators are practically frozen until the end of the violent part of the reaction. Moreover, this approximation is applied for clusterization routines only and, thus, does not affect the general nucleon dynamics in the PHQMD.

If one aims at a better quantitative description of lighter clusters or isotope yields, additional efforts are necessary. The binding energy of those clusters cannot be described by the Weizsäcker mass formula. This formula corresponds well to the cluster binding energies calculated by Skyrme type interactions [27], as will be discussed later, but shows shell effects and other quantum features. To study this, as well as the isotopic yields, the SACA algorithm is presently under improvement to include shell effects, symmetry energy, and pairing energy as well as the interaction between hyperons and nucleons [56]. Because the propagation of nucleons in PHQMD contains presently neither symmetry nor pairing energy terms we do not include these new features in this paper, with the exception of the hyperon-nucleon interaction which is taken as $2/3$ of the nucleon-nucleon interaction, assuming in this first study that the strange quark is inert. For the identification of the light clusters, $Z \leq 2$, we use MST.

We note that the consistent description of cluster production at high energies, where many resonances are excited, is an open issue. Due to that we avoid in this study applying

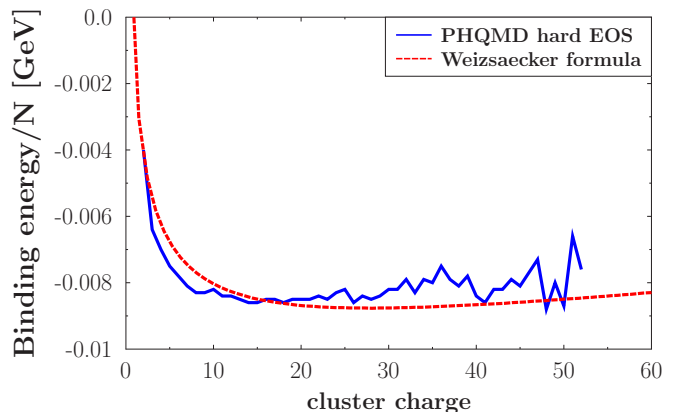


FIG. 4. Average binding energy of the clusters identified by the SACA algorithm from Au + Au collisions at $600A \text{ GeV}$ calculated within the PHQMD with the hard EoS as a function of the cluster charge calculated at late times ($150 \text{ fm}/c$).

SACA/MST at very early times when the matter is still resonance dominated; nevertheless even during the later expansion the presence of resonances has to be accounted for. To test their influence on the cluster yield we adopt the following procedure in the present calculations: (1) at the selected time, before the SACA/MST is applied, we let decay “virtually” the baryon resonances to nucleons and mesons. These decay nucleons are then taken into consideration for cluster formation in the SACA/MST algorithm (while the baryon resonances are propagated further in the PHQMD code until their natural decay). Under such an assumption we obtain a rather stable pattern of clusters in time with the SACA/MST algorithm. (2) We compare this with the cluster yield obtained if we do not include the nucleons from resonance “virtual” decays in SACA/MST, where we find fewer clusters (by 5–10%) at the early times of this study since fewer nucleons are available for clusterization. At later times the results are similar in both scenarios.

Further insight into cluster formation and the role of resonances can be obtained by employing a persistent coefficient which measures to which degree a cluster, measured at different times, contains the same nucleons. This will be the subject of an upcoming study.

B. QMD dynamics and cluster formation

One of the conditions for any reasonable approach to cluster formation is the requirement that the binding energy of clusters is reproduced. A too small binding energy means that the clusters are excited and emit further nucleons or α 's. Figure 4 shows the average binding energy of clusters at the end of a heavy-ion reaction of Au + Au at $600A \text{ GeV}$ as compared to the Weizsäcker mass formula. The clusters have been determined by the SACA algorithm. The binding energies do not vary for different beam energies and are stable from $75 \text{ fm}/c$ on. We see that for clusters with $Z \geq 5$ the binding energy is close to that expected from the Weizsäcker mass formula. This is all but self-evident. In PHQMD the density inside the clusters is given by the superposition of Gaussians

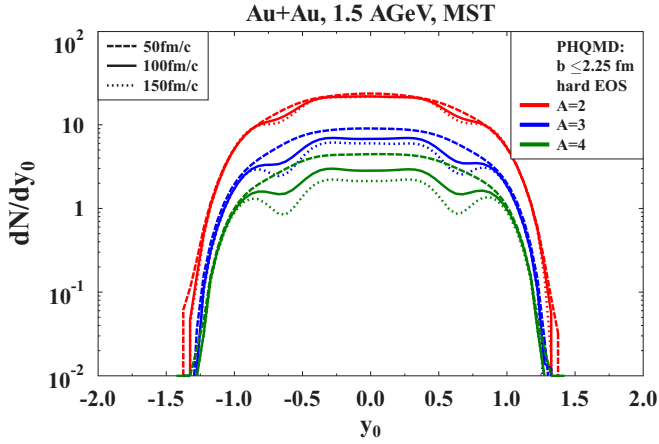


FIG. 5. Scaled rapidity distribution, $y_0 = y/y_{proj}$, of clusters with mass numbers $A = 2, 3, 4$ for central Au + Au collisions at 1.5A GeV calculated within the PHQMD approach. The clusters are determined by the MST algorithm at $t = 50$ fm/c, $t = 100$ fm/c, and $t = 150$ fm/c.

and there is no well defined surface. The binding energy is given by the expectation value of the Skyrme and Coulomb interaction for this spatial configuration supplemented by the total kinetic energy in the cluster rest system.

The nucleon and cluster rapidity distribution is another key observable which characterizes a heavy-ion collision. In Fig. 5 we display the scaled rapidity distribution $y_0 = y/y_{proj}$ (where y_{proj} is a projectile rapidity in the center-of-mass system) of light clusters of mass numbers $A = 2, 3, 4$ for central Au + Au reactions at $E_{beam} = 1.5A$ GeV. The clusters are determined by the MST algorithm at $t = 50$ fm/c, $t = 100$ fm/c, and $t = 150$ fm/c. We see that the cluster yields are rather stable versus time. We note that we find $\approx 10\%$ fewer clusters at 50 fm/c without accounting for nucleons from the “virtual” decay of resonances for the cluster formation, as discussed in Sec. III A.

Figure 6 presents the same scaled rapidity distribution of light clusters as in Fig. 5, but calculated within the mean-field dynamics of PHSD. One can see that the shape of the MF cluster distribution is rather different from that of QMD. Moreover, the MF cluster yield is not stable in time. This illustrates the limitation of the applicability of the mean-field dynamics for the cluster identifications. We observe furthermore that in the mean-field approach the clusters at midrapidity disappear early whereas those around projectile and target rapidity are longer present. This is expected because clusters at midrapidity are created by density fluctuations whereas those at projectile/target rapidity are mainly made of spectators which disintegrate slowly in mean-field approaches. The disappearance of fragments and, even more, the different times of disappearance raise questions about the applicability of coalescence models to mean-field calculations.

Figure 7 displays the multiplicity of clusters with $Z = 2-10$ for Au + Au collisions as a function of centrality, represented by the impact parameter, for two different energies, $E_{beam} = 600A$ MeV (upper plot) and $4A$ GeV (lower plot). At very central collisions most of the nucleons are unbound,

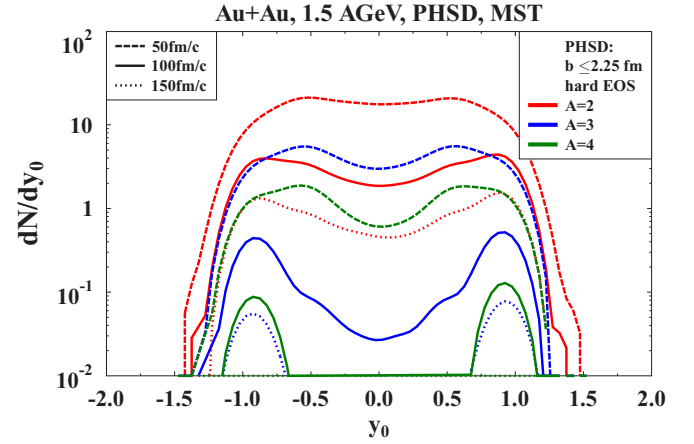


FIG. 6. Scaled rapidity distribution, $y_0 = y/y_{proj}$, of clusters with different mass numbers $A = 2, 3, 4$, for central Au + Au reactions at 1.5A GeV using the mean-field dynamics of the PHSD approach. The clusters are determined with the MST algorithm at $t = 50$ fm/c, $t = 100$ fm/c, and $t = 150$ fm/c.

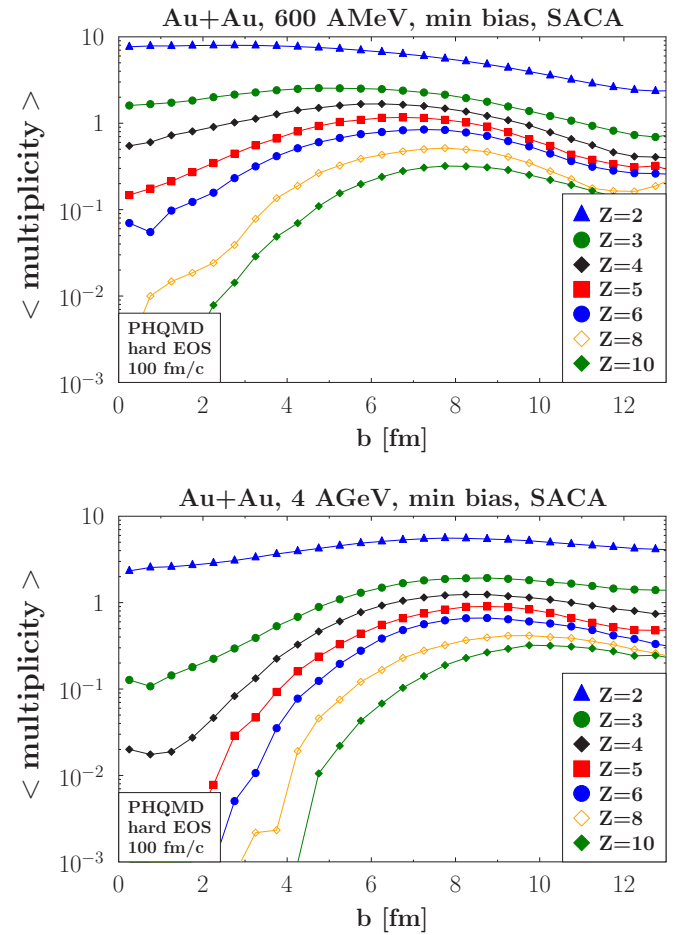


FIG. 7. Multiplicity of clusters with $Z = 2-10$ in Au + Au collisions as a function of the impact parameter for two different beam energies, $E_{beam} = 600A$ MeV (upper plot) and $4A$ GeV (lower plot) calculated within the PHQMD (hard EoS). The SACA algorithm is used to identify the clusters at time 100 fm/c.

however, even if some light clusters are produced whose number decreases with increasing beam energy. For larger impact parameters the intermediate mass clusters become important; they are mostly produced from the spectator matter. The general trend is similar for both energies but the multiplicities differ in detail. The origin of this difference is that the number of participant nucleons which enter the spectator matter and cause its instability, as well as the momenta of those nucleons, depend on the beam energy.

Another observable of interest is the in-plane flow, v_1 , described by the first coefficient of the Fourier expansion of the azimuthal distribution of nucleons or clusters,

$$\frac{dN}{d\phi} = N_0(1 + v_1 \cos \phi + 2v_2 \cos 2\phi + \dots). \quad (20)$$

The in-plane flow is created, on the one side, by the geometry of the reaction zone which allows hadrons with outward momentum to escape from the reaction zone (and therefore even in cascade calculations a finite v_1 is obtained) and, on the other side, by the transverse force, F_T . This force is proportional to the density gradient in transverse direction and is large at the interface between participant and spectator regions. The relative importance of both sources of v_1 (geometrical and interaction) depends on the cluster size. Light clusters come predominantly from the transition region between spectators and participants and show a larger v_1 around projectile rapidity than single nucleons, which come also from the high density participant region where the density gradient and therefore v_1 is smaller [9]. With increasing energy the passing time t_{pass} decreases but on the other side the density gradient, and hence the force F_T , becomes steeper. Both effects almost compensate for each other such that only a mild increase of $\Delta p_T = F_T t_{\text{pass}}$ occurs.

In Fig. 8 we show v_1 as a function of center-of-mass rapidity y for nucleons ($A = 1$) and clusters of different sizes ($A = 2, 3, 4$), created in Au + Au collisions at two beam energies, $E_{\text{beam}} = 600A$ MeV (upper plot) and $4A$ GeV (lower plot), for an impact parameter range of $4 \leq b \leq 6$ fm. One sees that v_1 increases with the mass number of the cluster. Even for light clusters v_1 differs significantly from that of protons and neutrons ($A = 1$), in particular the slope at midrapidity (which is often used to characterize the in-plane flow for the cases where only a limited rapidity interval can be measured) differs significantly for different A . The tendency that the large clusters (which have a higher probability to come from the spectator matter) show a large v_1 is found to be the same for both energies considered here; also the value of v_1 is similar. This mass dependence of the dynamical variables has also been found experimentally [84].

IV. RESULTS FOR HADRONIC SPECTRA

In this section we present the results of the PHQMD approach for the basic “bulk” observables like the rapidity distribution and the transverse mass m_T spectra of hadrons—protons, antiprotons, pions, (anti)kaons and (anti)lambdas at a variety of energies—from SIS to top RHIC energies, and we confront our results with the experimental data. All rapidities are measured in the center of mass of the nucleus-nucleus

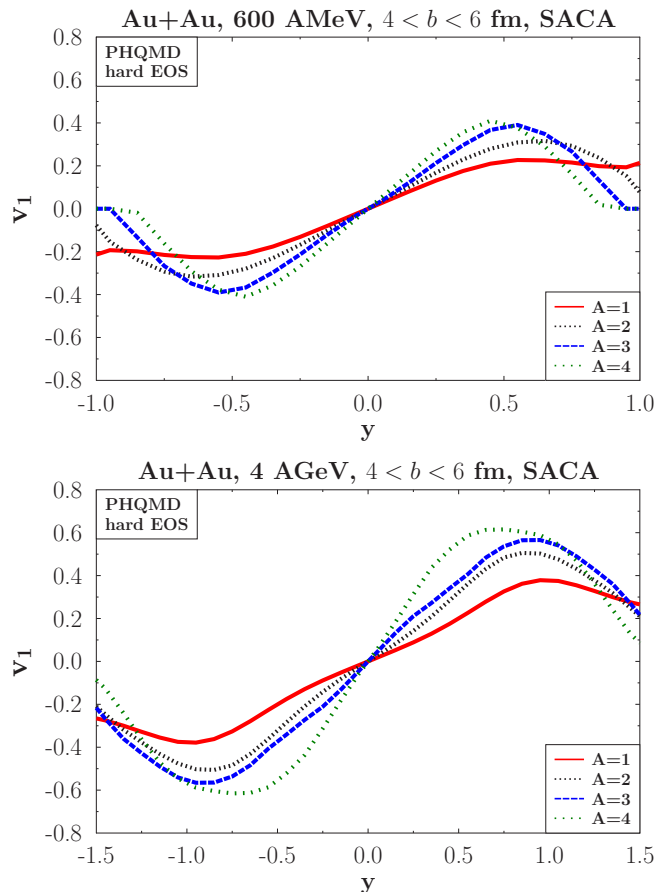


FIG. 8. The in-plane flow, v_1 , as a function of the rapidity y for nucleons ($A = 1$) and clusters with mass numbers $A = 2, 3, 4$ for Au + Au collisions at beam energies of $600A$ MeV ($y_{\text{proj}} = 0.539$), upper plot, and of $4A$ GeV ($y_{\text{proj}} = 1.17$), lower plot, for an impact parameter range of $4 \leq b \leq 6$ fm calculated within the PHQMD (hard EoS) using the SACA algorithm for cluster recognition.

system. We recall that the “bulk” observables have been extensively investigated in many PHSD studies, and a good agreement for a variety of “bulk” observables as well as for the collective flows v_n , electromagnetic observables, heavy flavor, etc., have been reported; cf. [39,50–53]. However, it is necessary to verify the “bulk” dynamics within the novel PHQMD approach because the initialization of the nucleus as well as the nucleon dynamics are realized differently. In this respect the PHQMD provides a unique possibility to explore the differences between the mean-field and the quantum-molecular dynamics since both are realized in the framework of the same PHQMD code, i.e., both propagations can be tested while implying the collision integral of PHSD. This allows to investigate how a different realization of the potential interaction—MF versus QMD—may modify the trajectories of the individual nucleons in phase space. Also the interacting Gaussian wave functions in QMD with a given width have a different time evolution as compared to pointlike nucleons in a meanfield. In addition we explore the influence of the EoS—hard vs soft—realized with a static density dependent potential in the QMD mode as discussed in Sec. II C.

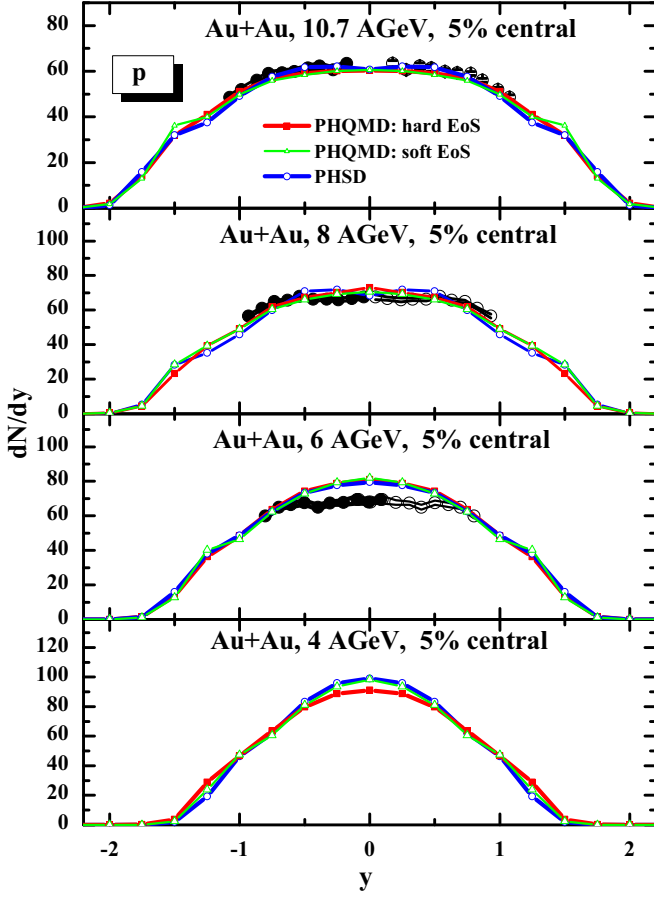


FIG. 9. The rapidity distributions of protons for 5% central Au + Au collisions at 4A, 6A, 8A, 10.7A GeV (plots from lower to upper). The experimental data have been taken from Ref. [85]. The full symbols correspond to the measured data, whereas the open symbols are the data reflected at midrapidity. Solid red lines with open squares refer to the PHQMD results with a hard EoS, the green lines with open triangles are PHQMD results with a soft EoS, and the blue lines with open circles are the PHSD results.

A. AGS energies

We start our comparison by showing in Figs. 9 and 10 the proton rapidity distributions and m_T spectra for central Au + Au collisions at beam energies of 4A, 6A, 8A, and 10.7A GeV, calculated in PHQMD with a hard and a soft EoS. The PHQMD results are compared with those from PHSD as well as with the Alternating Gradient Synchrotron (AGS) experimental data [85–91]. In the rapidity spectra the influence of the EOS becomes only slightly visible at the lowest beam energy, but the transverse mass spectra show a sensitivity to the EOS at all energies. A hard EOS increases the slope of the spectra at large m_T and lowers the yield at low m_T as compared to a soft EoS. We find that the PHQMD with soft EoS agrees very well with the PHSD result. This agreement with experiment allows us to conclude that the stopping of the nuclei in PHQMD is reasonably described. This is important for the interpretation of the results for the newly produced hadrons, since their abundances are sensitive to the energy loss of the initial colliding nucleons, i.e., to the

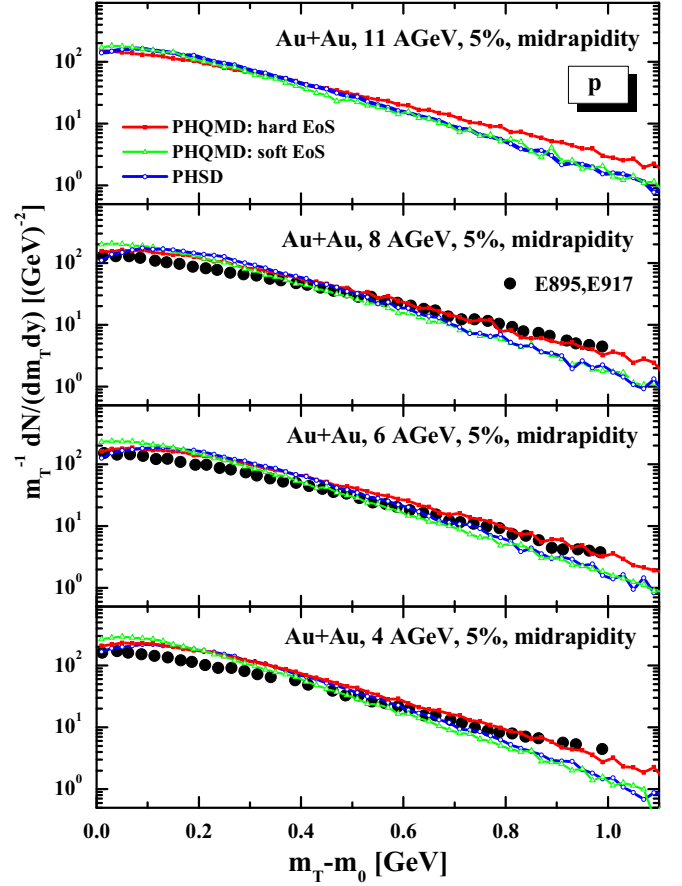


FIG. 10. The transverse mass m_T spectra of protons at midrapidity for 5% central Au + Au collisions at 4A, 6A, 8A, 10.7A GeV (plots from lower to upper). The experimental data have been taken from Ref. [85]. Solid red lines with open squares refer to the PHQMD results with a hard EoS, the green lines with open triangles are the PHQMD results with a soft EoS, and the blue lines with open circles are the PHSD results.

fraction of their kinetic energy which will be converted into mass production.

In Figs. 11 we display the rapidity distribution and in Fig. 12 the m_T spectra of π^+ , K^+ , K^- , and $\Lambda + \Sigma^0$, produced in central Au + Au collisions for different beam energies, $E_{lab} = 4A, 6A, 8A,$ and $10.7A$ GeV. Again we compare here the PHQMD calculations with a soft and a hard EoS with the PHSD results (we note that for the m_T spectra we show only hard PHQMD and PHSD results for clearer presentation). Contrary to the proton m_T spectra, which show a visible sensitivity to the EoS, the spectra of newly produced hadrons indicate only a very mild dependence on the nucleon potential: all cases are rather similar to each other.

B. SPS energies

Now we step up in energy and confront the PHQMD approach with the NA49 experimental data at Super Proton Synchrotron (SPS) energies. Again we start with checking the stopping of protons. The proton rapidity spectra and m_T spectra of PHQMD at $E_{beam} = 20A, 30A, 40A, 80A,$ and

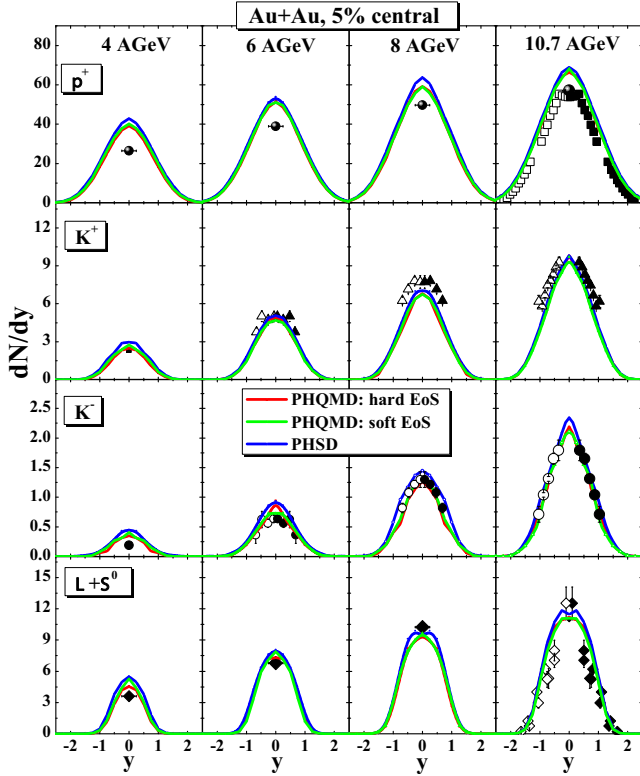


FIG. 11. The rapidity distributions of π^+ , K^+ , K^- , and $\Lambda + \Sigma^0$ for 5% central Au + Au collisions at 4A, 6A, 8A, and 10.7A GeV (plots from left to right) in comparison to the experimental data from Refs. [86–91]. Solid red lines with open squares refer to PHQMD results with a hard EoS, the green lines with open triangles are the PHQMD results, with a soft EoS, and the blue lines with open circles are the PHSD results.

158A GeV, in comparison with the experimental data [92–94], are displayed in Figs. 13 and 14. Here the solid red lines with open squares represent the PHQMD results with a hard EoS. The PHQMD proton rapidity distribution and the m_T spectra show a reasonable agreement with experimental data, thus the QMD dynamics provide also a correct stopping at SPS energies similar to those at the AGS.

In Figs. 15 and 16 the y distributions and m_T spectra of π^+ , K^+ , K^- , and $\Lambda + \Sigma^0$ for 5% central Au + Au collisions at 20A, 40A, 80A, and 158A GeV are presented in comparison to the experimental data from the NA49 Collaboration [92–94]. Here we find that the PHQMD agrees with the experimental data—similarly to the PHSD—since the dynamics of newly produced hadrons at high energies is dominated by the collision integral and is not very sensitive to the realization of nucleon dynamics, via MF or QMD.

C. RHIC BES energies

Recent experimental measurements by the STAR Collaboration within the RHIC BES program provide high precision experimental data at midrapidity. Here we present selected results for the comparison of PHQMD with RHIC BES data. A more systematic study on this issue is in preparation.

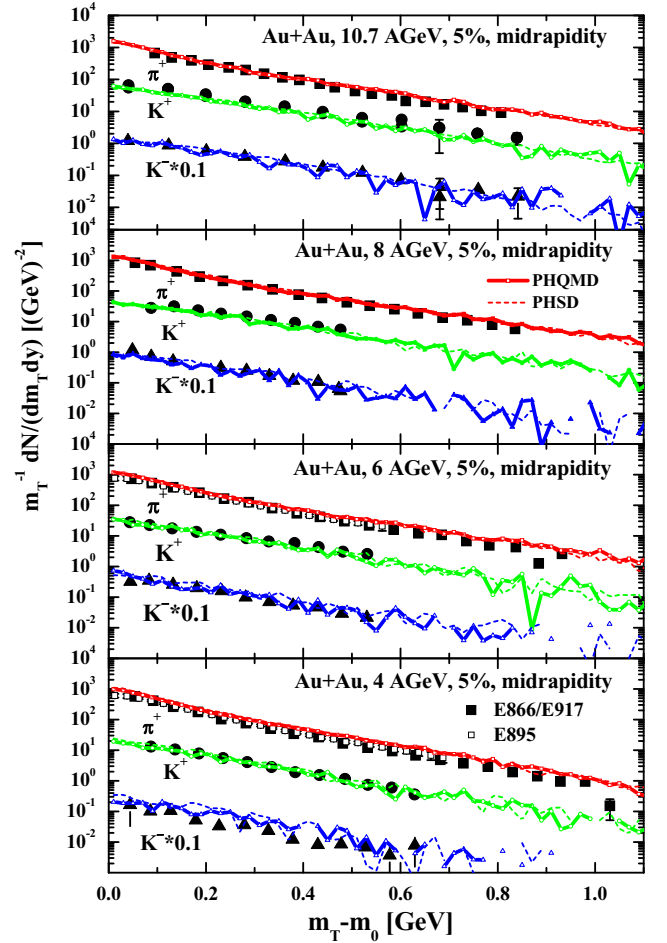


FIG. 12. The transverse mass m_T spectra of π^+ , K^+ , K^- , and $\Lambda + \Sigma^0$ at midrapidity for 5% central Au + Au collisions at 4A, 6A, 8A, and 10.7A GeV (plots from lower to upper) in comparison to the experimental data from Refs. [86–91]. Solid lines with open symbols refer to PHQMD results with a hard EoS and the dashed lines are the PHSD results.

Figure 17 shows the transverse momentum spectra of produced mesons π^\pm , K^\pm , protons, and antiprotons at midrapidity for different centrality classes, measured by the STAR Collaboration for Au + Au at $\sqrt{s} = 11.5$ GeV [95]. The PHQMD calculations correspond to the hard EoS. We find that also the centrality dependence of the spectra of newly produced particles is well described in the PHQMD approach while the proton slope is slightly underestimated at large p_T . A similar tendency has been observed for protons at SPS energies; cf. Fig. 13.

D. Top RHIC energy

This good agreement between the PHQMD results for the single-particle rapidity and transverse momentum spectra and the experimental data continues for higher beam energies. In Figs. 18 and 19 we show the calculated rapidity distributions and transverse momentum p_T spectra of hadrons (π^\pm , K^\pm , p , \bar{p} , $\Lambda + \Sigma^0$, $\bar{\Lambda} + \bar{\Sigma}^0$) for 5% central Au + Au collisions at $\sqrt{s} = 200$ GeV in comparison to the

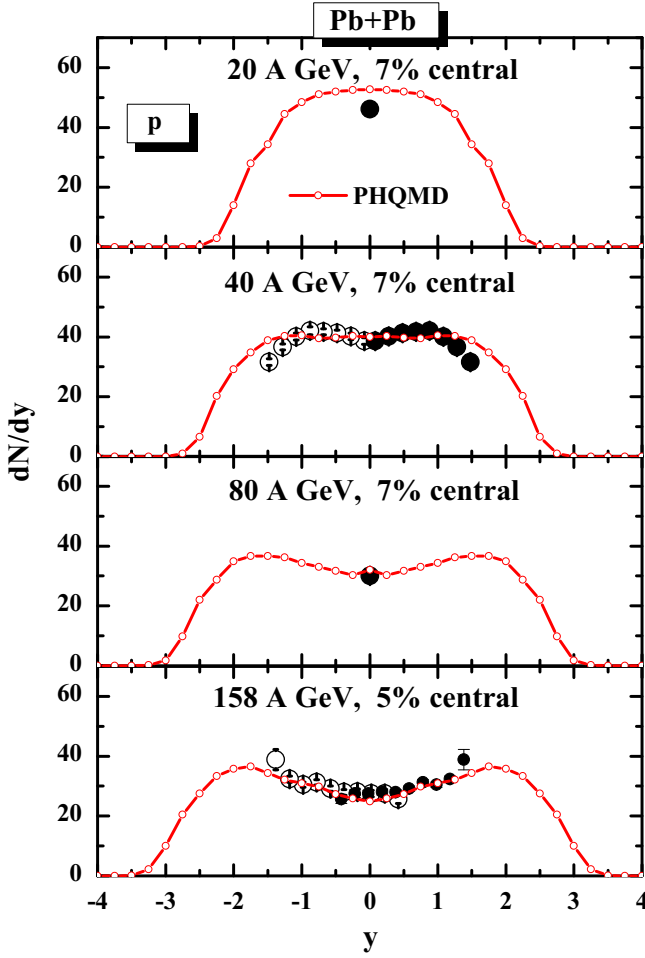


FIG. 13. The rapidity distributions of protons at midrapidity for 5% central Pb + Pb collisions at 20A, 40A, 80A, and 158A GeV (plots from upper to lower). The experimental data have been taken from Refs. [92–94]. The full symbols correspond to the measured data, whereas the open symbols are the data reflected at midrapidity. Solid red lines with open squares refer to PHQMD results with a hard EoS.

experimental data from the BRAHMS [96,97], PHENIX [98], and STAR [99] Collaborations.

We note again that at RHIC energies we show only the PHQMD calculations since the PHSD and PHQMD give very similar results. At such ultrarelativistic energies the influence of the nucleon potential is negligible and the shape of the spectra (even for protons) is mainly defined by the partonic interactions. We note that at the highest energy, PHQMD (as well as the PHSD) underpredicts the spectra at high p_T . That can be attributed to the fact that some parts of the initial “hard” processes are partially smeared out in the present realization of the PHSD by the melting of “prehadrons” from the strings to massive dressed quasipartons in line with the DQPM model. By that procedure some minijets, present in the LUND strings, can be melted to the QGP, too. This issue requires further investigation which we leave for future studies.

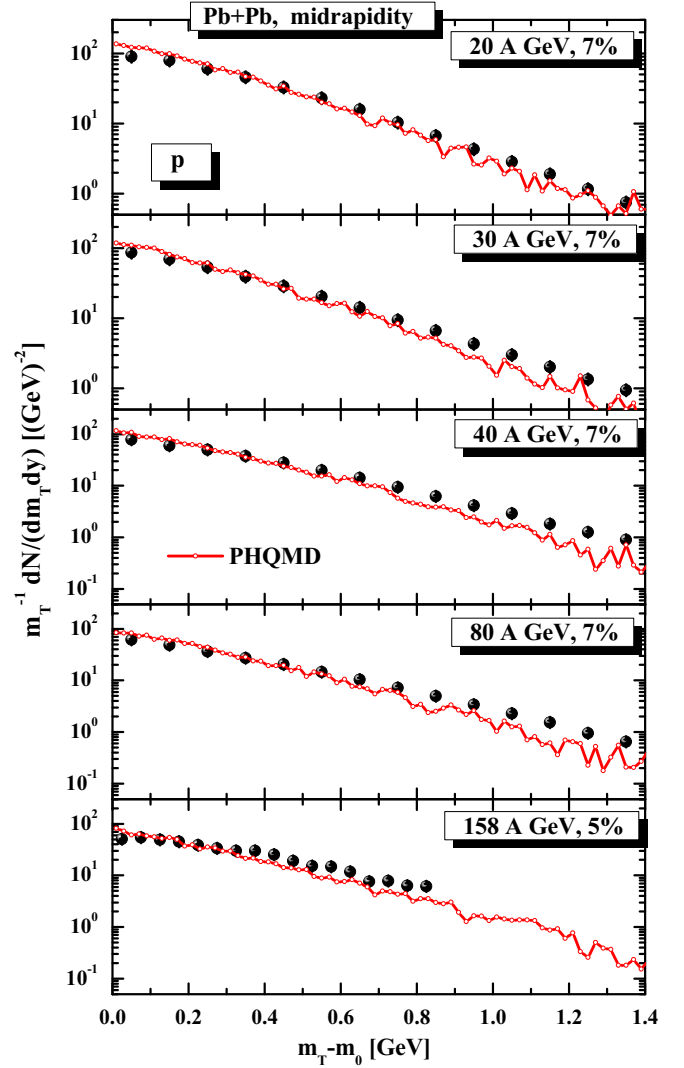


FIG. 14. The transverse mass m_T - spectra of protons for 5% central Pb + Pb collisions at 20A, 30A, 40A, 80A, and 158A GeV (plots from upper to lower), in comparison to the experimental data from NA49 Collaboration from Refs. [92–94]. Solid red lines with open squares refer to PHQMD results with a hard EoS.

E. SIS energies

We close this section by going down in energy to SIS energies, which allows us to show the sensitivity of newly produced particle spectra to the QMD and MF dynamics as well as to the different EoS. We start with the pion spectra since—as discussed in the introduction—the proton spectra can be compared to the data only after the subtraction of the protons bound in the clusters. We will see in the next section that the fraction of such bound protons is rather high at low energies since the cluster production grows with decreasing bombarding energy.

At $E_{\text{beam}} = 1.5A$ GeV the pion rapidity spectra as a function of $y_0 = y/y_{\text{proj}}$ in central Au + Au reactions have been measured by the FOPI Collaboration [100]. In Fig. 20 we compare the FOPI data with PHQMD calculations employing a hard (solid lines with squares) and a soft EoS (dashed lines

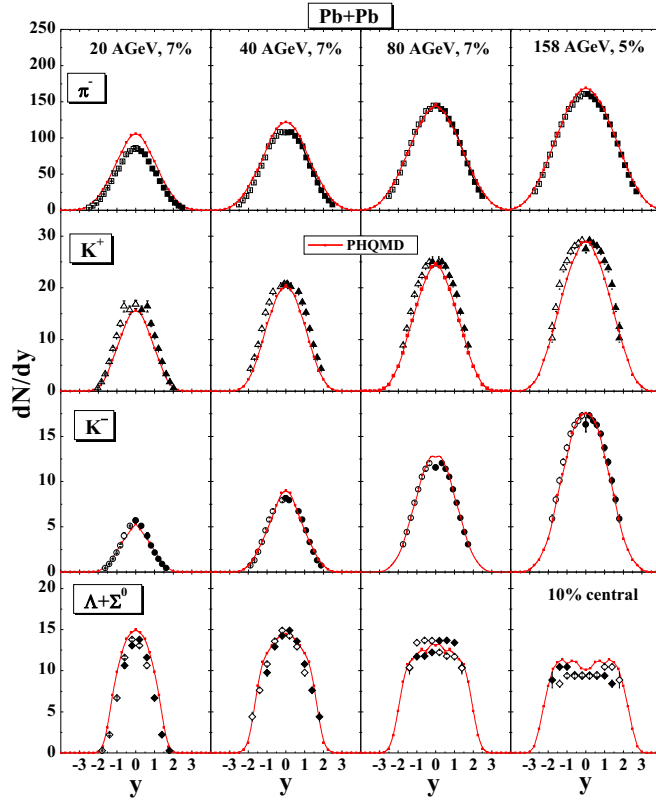


FIG. 15. The rapidity distributions of π^+ , K^+ , K^- , and $\Lambda + \Sigma^0$ from PHQMD for 5% central Au + Au collisions at 20A, 40A, 80A, and 158A GeV (plots from left to right) in comparison to the experimental data from the NA49 Collaboration [92–94].

with triangles) as well as with the PHSD results (dotted lines with stars). As seen from Fig. 20, the pion rapidity distribution is sensitive to the EoS: the experimental data are in best agreement with the PHQMD results for a hard EoS. The softening of the EoS leads to a small enhancement of the pion yield as seen for the PHQMD results with a soft EoS as well as for the PHSD results, where the EoS is also soft.

Finally, we can conclude from this comparison that the rapidity as well as the m_T spectra of produced particles, as well as of protons, are well reproduced in the PHQMD approach. This means also that the basic features like energy loss and elementary cross sections are under control. These findings allow us to proceed to investigate the cluster production based on the SACA and MST algorithms, which we present in the next section.

V. RESULTS FOR CLUSTERS

A. Light clusters

At lower beam energies cluster production becomes important. According to the measurements by the FOPI Collaboration [100] in central Au + Au collisions at 1.5A GeV about 111 free protons are found and 60 protons are bound mostly in $Z = 1, 2$ clusters. In Fig. 21 we compare the PHQMD results for the scaled rapidity distributions ($y_0 = y/y_{\text{proj}}$ with y_{proj} being the beam rapidity in the center-of-mass frame) of the

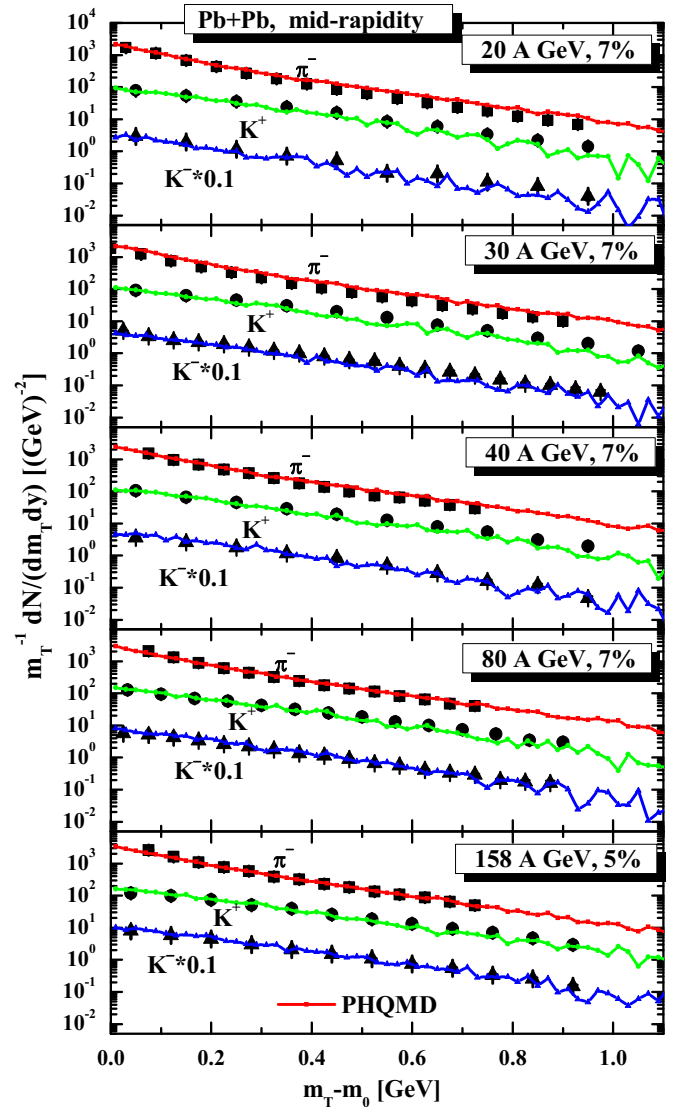


FIG. 16. The transverse mass m_T spectra of π^+ , K^+ , K^- , and $\Lambda + \Sigma^0$ at midrapidity from PHQMD for 5% central Au + Au collisions at 20A, 30A, 40A, 80A, and 158A GeV (plots from upper to lower) in comparison to the experimental data from the NA49 Collaboration [92–94].

$Z = 1$ “clusters” (which includes unbound protons as well as light clusters as deuterons and tritons) and the (unbound) protons with FOPI experimental data for central Au + Au collisions at 1.5A GeV [100]. Here we present the results for clusters identified by MST (red dotted line) or by SACA (red dashed line). Since the integrated yield of the $Z = 1$ clusters gives almost the total number of charges (there are on the average only 6.8 clusters with $Z = 2$), it is expected the integrated PHQMD $Z = 1$ yield agrees with data. In addition, also the scaled rapidity distribution of $Z = 1$ “clusters,” which reflects the stopping, is well reproduced. This is one of the reasons that also the rapidity distributions of the produced particles, like that of π^+ and π^- , agree with experiments (cf. Fig. 20). In Fig. 21 we show also the rapidity distribution of free protons (blue lines). The difference between the rapidity

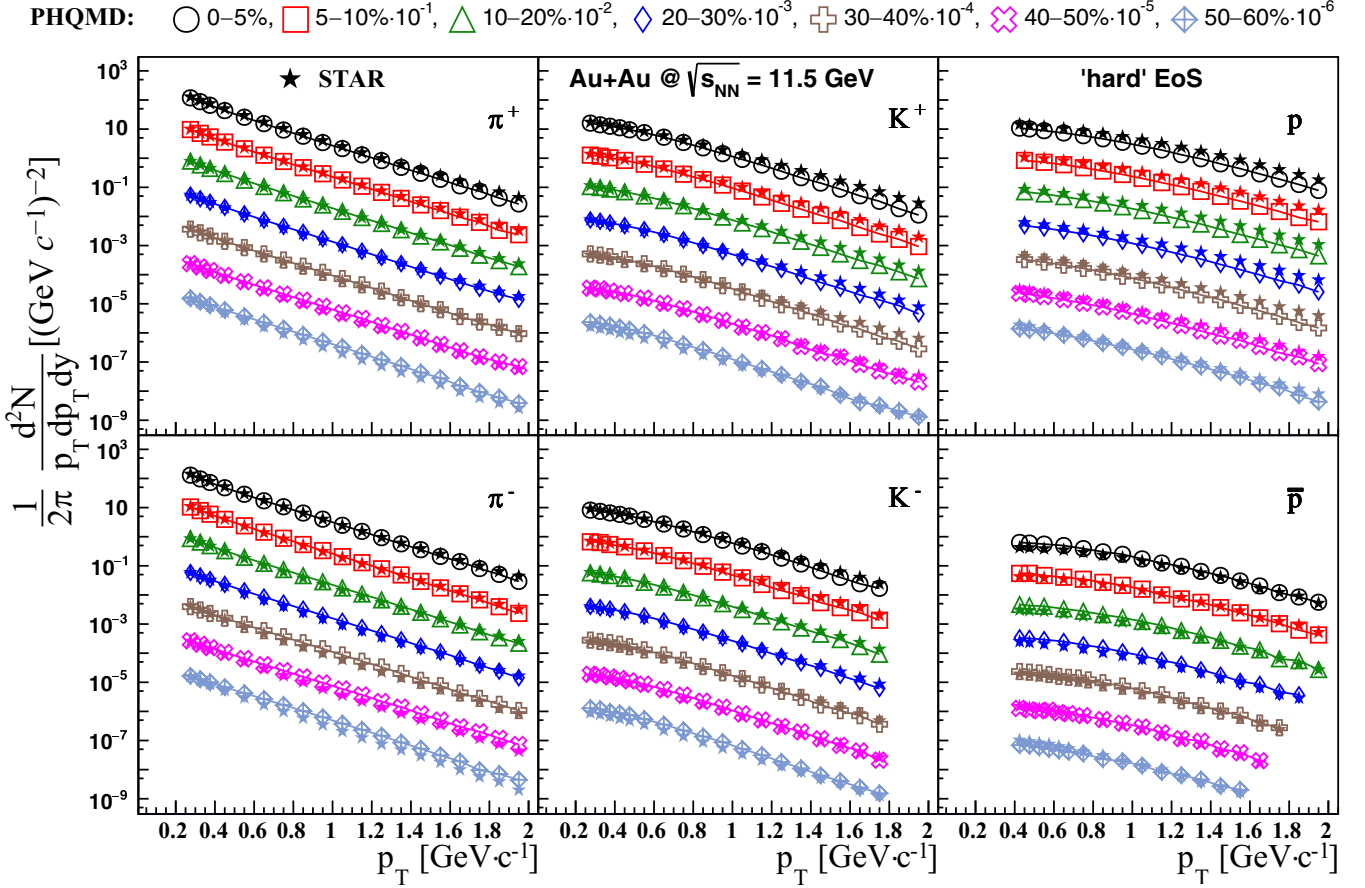


FIG. 17. The midrapidity p_T spectra of π^\pm , K^\pm , p , and \bar{p} at midrapidity for Au + Au at $\sqrt{s} = 11.5$ GeV from PHQMD with hard EoS in comparison to the STAR experimental data from Ref. [95] for different centrality classes. The spectra for different centralities are multiplied by corresponding factors for better visibility: 0–5% $\times 1$; 5–10% $\times 10^{-1}$; 10–20% $\times 10^{-2}$; 20–30% $\times 10^{-3}$; 30–40% $\times 10^{-4}$; 40–50% $\times 10^{-4}$; 50–60% $\times 10^{-6}$.

distribution of $Z = 1$ (red lines) and protons (blue lines) in Fig. 21 is due to those protons which are bound in $Z = 1$ clusters.

As discussed already in Sec. III, SACA with Skyrme type interactions only—as presently implemented in the PHQMD—(blue long dashed line) is not very efficient for describing the light clusters at midrapidity and, correspondingly, underestimates the number of nucleons which are bound in clusters. The MST algorithm—which does not account for the binding energy of clusters as SACA and, thus, is less sensitive to the potential interaction of nucleons—(blue short-dashed line in Fig. 21) comes much closer to the data, in spite of disregarding the quantum nature of light clusters. Moreover, as demonstrated in Fig. 5 and discussed in Sec. III B, the MST algorithm provides rather a stable yield of light clusters over time. Therefore, for further analysis of light clusters at midrapidity in this section we employ the MST algorithm.

We step to high energies and confront expectations from PHQMD for light clusters with the available experimental data at AGS energies. In Fig. 22 the PHQMD results with hard EoS of the invariant multiplicities for p , d , t , ^3He , ^4He at $p_T \leq 0.1$ GeV as function of rapidity y at 10% cen-

tral (upper plot) and minimum bias (lower plot) Au + Au collisions at $E_{\text{beam}} = 11A$ GeV are compared to the experimental data from the E878 [102] and E886 [101] Collaborations, labeled by different symbols for the various species. For ^4He we represent separately the measurements from E886 (empty triangles) and E878 (filled triangles). The clusters are identified by the MST method and later selected through the physical isospin and charge combinations. The colored lines in Fig. 22 are the PHQMD results, which we provide also with uncertainties which resemble the statistical fluctuations of the binned distributions. As one can see they are in line with the measured experimental data. We point out that in the final stage of heavy-ion reactions the MST algorithm finds approximately the same number of light clusters which are recognized in a rather stable and time-independent way by the SACA method.

Finalizing this section, we stress that the PHQMD is a consistent microscopic transport approach applicable to relativistic energies in which clusters are produced dynamically by the same potential interaction which governs the time evolution of the nucleons up to the end of the reaction. Furthermore, the cluster finding algorithm (MST) applied at different time finds a similar cluster pattern. No assumptions about a

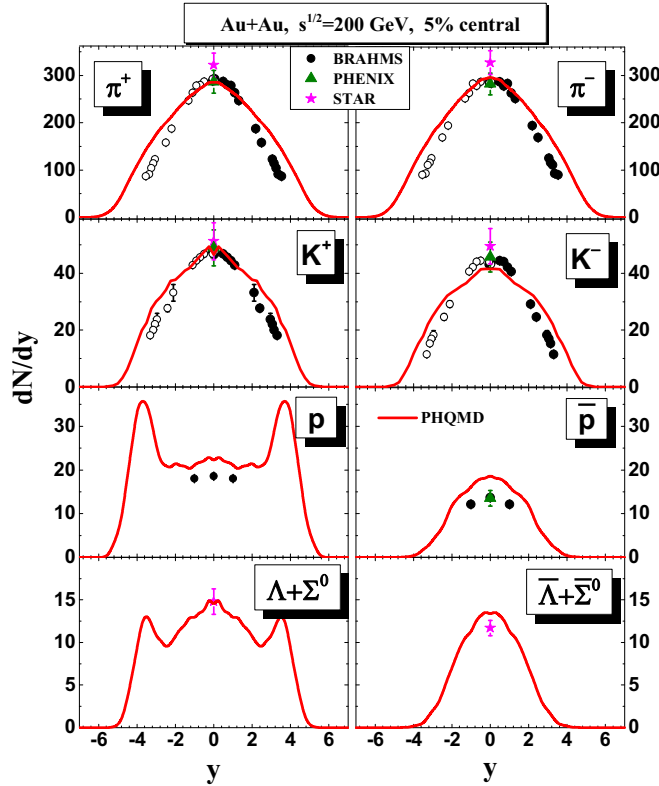


FIG. 18. The rapidity distributions of π^+ , K^+ , p , and $\Lambda + \Sigma^0$, left, and their antiparticles π^- , K^- , \bar{p} , and $\bar{\Lambda} + \bar{\Sigma}^0$, right, for 5% central Au + Au collisions at $\sqrt{s} = 200$ GeV in comparison to the experimental data from the BRAHMS [96,97], PHENIX [98], and STAR [99] Collaborations.

coalescence time or coalescence radii are necessary in order to obtain these clusters. They are naturally produced by the interactions among the nucleons during the entire heavy-ion reaction.

Generally, the existence of light clusters at midrapidity of heavy-ion collisions is an amazing phenomenon. There the participating nucleons form a fireball which can well be described in thermal approaches assuming a temperature of the order of 100 MeV [103]. Also the transverse energy spectra show an inverse slope parameter of this order which is, however, composed of a radial flow and a thermal contribution. This observation has triggered the suggestion that in high energy heavy-ion reactions a hot thermal system is formed. On the other hand, the light clusters which are formed have binding energies of a couple of MeV and they cannot survive in such a hot environment. In addition, any collision of a cluster with hadrons from the fireball would destroy these clusters. It is, therefore, an open question how these midrapidity clusters, which can be observed up to the highest LHC beam energies, are formed and how they can survive in this hot fireball. Static models like the coalescence model or the statistical model cannot answer this question. The PHQMD results obtained with the MST cluster identification method show that clusters can be formed in such an environment, but the MST method does not allow for a detailed investigation of why and when clusters are formed since this method can

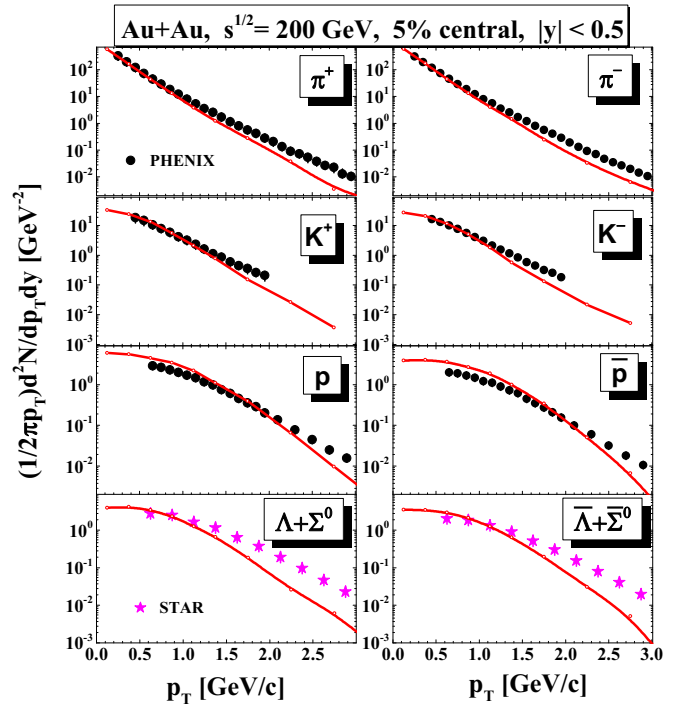


FIG. 19. The transverse momentum p_T spectra of π^+ , K^+ , p , and $\Lambda + \Sigma^0$, left, and their antiparticles π^- , K^- , \bar{p} , and $\bar{\Lambda} + \bar{\Sigma}^0$, right, for 5% central Au + Au collisions at $\sqrt{s} = 200$ GeV in comparison to the experimental data from the PHENIX [98] and STAR [99] Collaborations.

identify clusters only at the end of the reaction. In order to overcome this limitation, further development of the SACA algorithm for finding light clusters is required which will help to shed light on the dynamical formation of the light clusters.

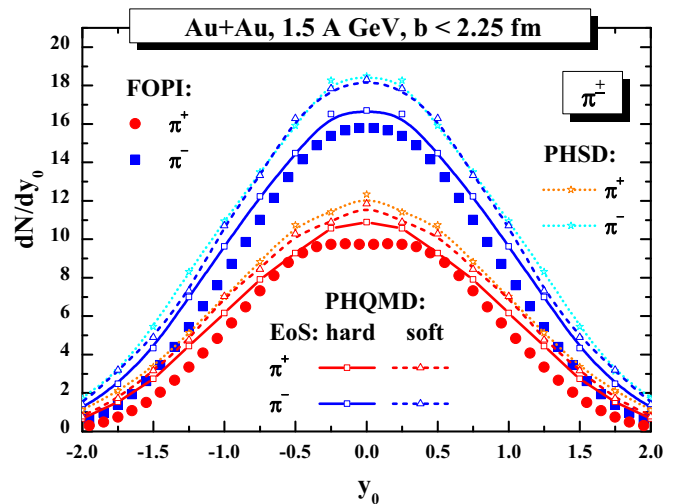


FIG. 20. Scaled experimental rapidity distribution, $y_0 = y/y_{proj}$, of π^+ and π^- observed in central Au + Au reactions at 1.5A GeV [100] in comparison with PHQMD calculations with a hard (solid lines with squares) and a soft EoS (dashed lines with triangles) as well as with the PHSD result (dotted lines with stars).

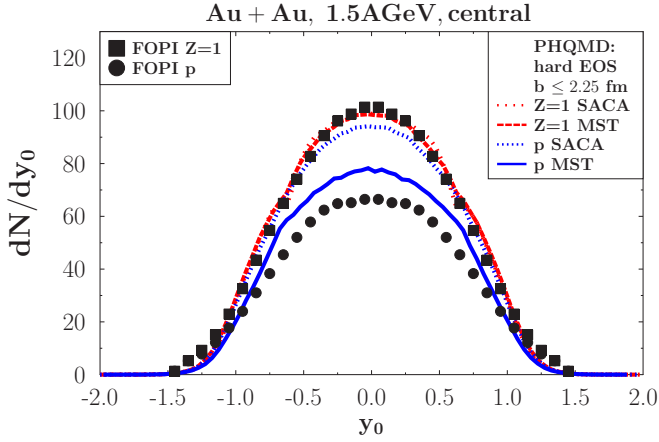


FIG. 21. Scaled experimental rapidity distribution, $y_0 = y/y_{\text{proj}}$, of all bound and unbound protons ($Z = 1$), solid squares, and free (unbound) protons, solid dots, observed by the FOPI Collaboration in central Au + Au collisions at 1.5 A GeV [100] in comparison to the PHQMD results: the rapidity distribution of all bound and unbound protons ($Z = 1$) after the clusters have been identified by MST (red dotted line) or by SACA (red dashed line); the rapidity distributions of free protons after subtracting the protons bound in clusters identified by MST (blue solid line) or by SACA (blue short dotted line).

B. Heavy clusters

In the past, QMD approaches have been very successfully applied to describe many details of the cluster formation at energies below $E_{kin} = 200A$ MeV [8,58,60,83]. They could reproduce charge yields, cluster multiplicities, cluster spectra, and complex phenomena like bimodality. At these energies the fragmentation of spectator matter is the dominant mechanism for cluster production, and cluster identification methods like the minimum spanning procedure or the SACA method could identify the produced cluster [54,55].

Within the PHQMD we extend our research to slightly higher energies and confront first the PHQMD results to the experimental data of the ALADIN Collaboration, which has measured the cluster formation at beam energies between 600A and 1000A MeV [6,7]. This is presently the highest beam energy for which experimental data on heavy clusters are completely analyzed. For this investigation we use a hard EoS and employ the SACA algorithm. One of the key results of the ALADIN Collaboration is the “rise and fall” of the multiplicity of intermediate mass clusters, $3 \leq Z \leq 30$, emitted in the forward direction. This multiplicity is presented as a function of the sum of all forward emitted bound charges, $Z_{\text{bound}2}$ which can be expressed with help of the Θ function:

$$Z_{\text{bound}2} = \sum_i Z_i \Theta(Z_i - (1 + \epsilon)),$$

with ($\epsilon < 1$). One obtains a distribution which is for Au projectiles almost independent of the beam energy in the interval $600A \leq E_{\text{beam}} \leq 1000A$ MeV and also independent of the target size. We note that in the original publication [6] the intermediate mass cluster multiplicity was overestimated due to misidentified, mostly $Z = 3$, clusters which were in

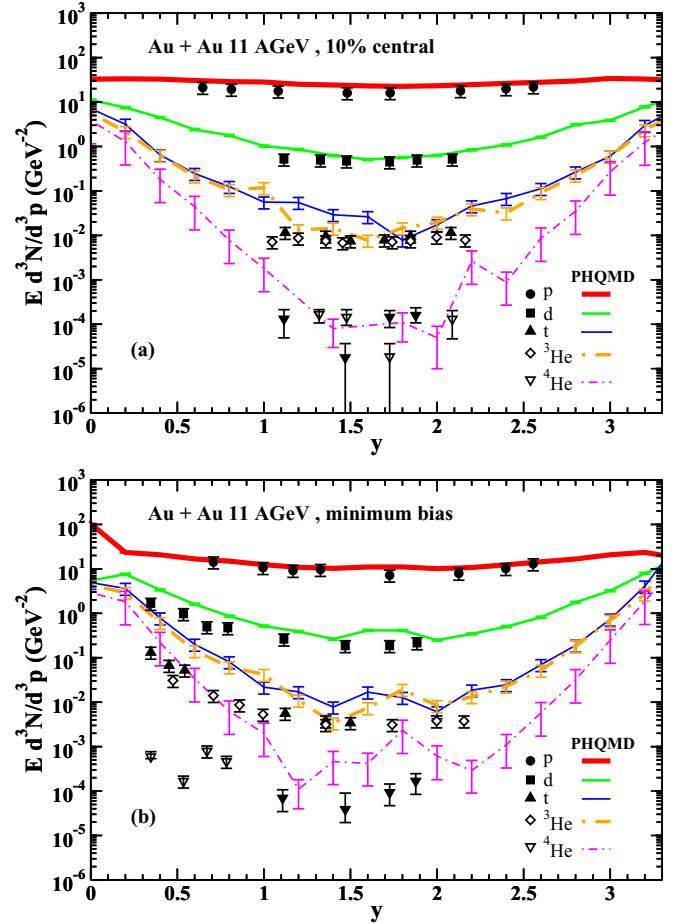


FIG. 22. The invariant multiplicities for $p, d, t, {}^3\text{He}, {}^4\text{He}$ at $p_T \leq 0.1$ GeV versus rapidity for 10% central (upper plot) and minimum-bias (lower plot) Au + Au collisions at $E_{\text{beam}} = 11A$ GeV. Experimental data from E886 and E878 Collaborations are taken from Refs. [101,102]. The solid (dash-dotted) lines with different thicknesses correspond to the PHQMD calculations with hard EoS for charge value $Z = 1$ ($Z = 2$). Clusters are identified by the MST algorithm.

reality two α particles. Later, with an improved apparatus, this was realized for smaller systems. A remeasurement for the Au + Au system has shown that the multiplicity of intermediate mass clusters is about 15% lower than that published in [6]. The corrected rise and fall curve for Au + Au reactions has been published in [104] and will be used for the comparison in our study.

In Fig. 23 we display our results for Au + Au at 600A MeV calculated with a hard EoS in comparison with minimum bias ALADIN data [104]. The clusters identified by SACA are stable for time larger than 50 fm/c as shown in Fig. 23. One can see clearly that PHQMD with a hard EoS reproduces quite nicely the experimentally observed “rise and fall.”

The rise and fall of the intermediate mass cluster multiplicity depends strongly on the nuclear equation of state. In Fig. 24 we show the rise and fall for a soft EoS. There in semiperipheral and peripheral collisions, where $Z_{\text{bound}2}$ is large, the spectator matter is much less stable and fragments

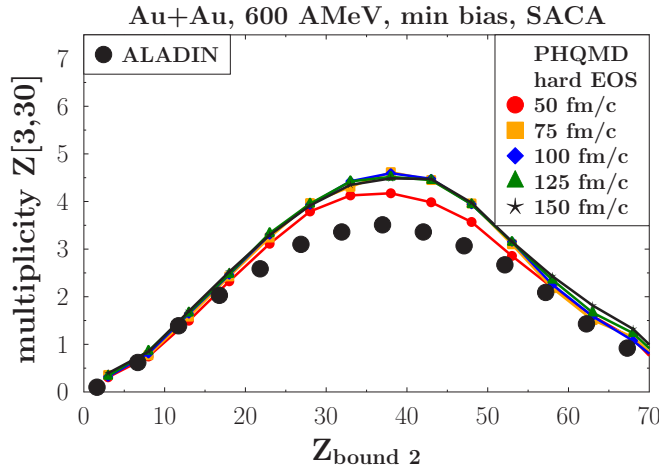


FIG. 23. “Rise and fall” of the multiplicity of clusters with $Z \in [3, 30]$ as a function of the total bound charge $Z_{\text{bound } 2}$. Both quantities are measured for forward emitted clusters. The experimental data of the ALADIN Collaboration are from Ref. [56,104]. The plot shows the PHQMD results with hard EoS using cluster identification by SACA for 600A GeV at different times: 50 (red line), 75 (orange line), 100 (blue line), 125 (green line), and 150 (black line) fm/c.

into a much larger number of intermediate mass clusters as compared to a hard EoS (Fig. 23). The fragment pattern in semiperipheral reactions can therefore serve as an additional observable to determine the hadronic EoS experimentally.

The ALADIN Collaboration has also measured the multiplicity of clusters of a given charge Z ($Z = 3, 4, 5, 7, 10$) as a function of $Z_{\text{bound } 2}$. The PHQMD results are compared with the experimental finding in Fig. 25. Due to the arguments presented above we have multiplied the multiplicity of $Z = 3$ clusters, published in [6], by 0.85, assuming that the misidentified clusters were exclusively $Z = 3$ clusters. We observe a quite good agreement of the PHQMD results with experimental data.

Figure 26 shows the charge of the largest cluster as a function of Z_{bound} for forward emitted clusters in Au + Au

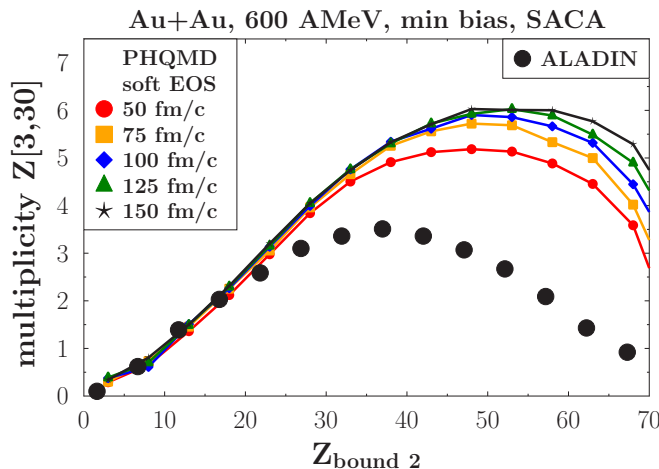


FIG. 24. Same as Fig. 23, but for a soft EoS.

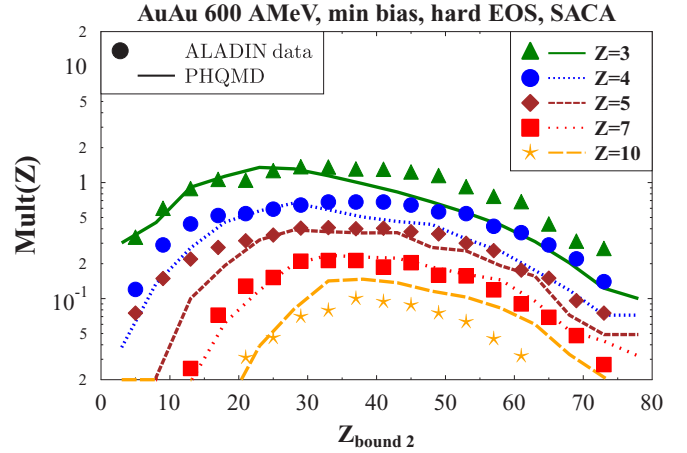


FIG. 25. “Rise and fall” of the multiplicity of intermediate mass clusters of a given charge Z ($Z = 3, 4, 5, 7, 10$) as a function of the total bound charge $Z_{\text{bound } 2}$. Both quantities are measured for forward emitted clusters. The results of PHQMD with cluster identification by SACA (lines) are compared to the ALADIN experimental data [6] (symbols). The $Z = 3$ data are corrected by 15%; see text.

collisions at 600A MeV. In central collisions, where Z_{bound} is small, we see also no large clusters, whereas in very peripheral reactions $Z_{\text{bound } 2}$ approaches the charge of the projectile. The PHQMD calculations with the SACA algorithm for cluster identification reproduce the experimental data. Even more importantly, the result does not depend on the time when we apply the SACA algorithm because the cluster pattern changes only little with time.

From Figs. 25 and 26 we can conclude that PHQMD describes the size and the multiplicity of clusters $Z \geq 2$ from very central to peripheral Au + Au reactions at 600A MeV if the SACA algorithm is employed. Beyond $E_{\text{beam}} = 1A$ GeV (where the cluster distribution is very similar to the more

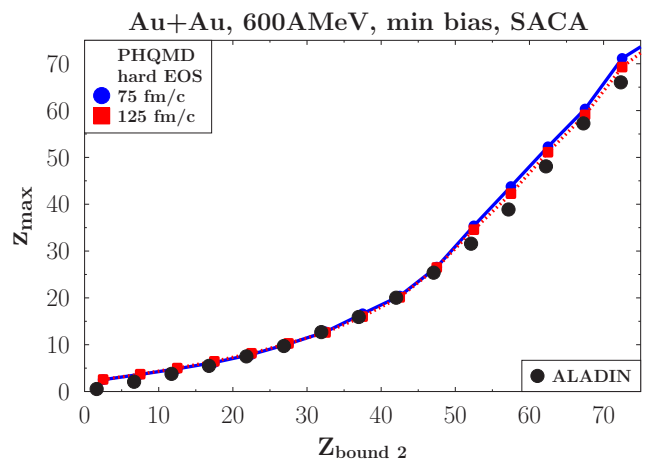


FIG. 26. The average charge of the largest cluster as a function of the total bound charge. Both quantities are measured for forward emitted clusters. The PHQMD results with cluster identification by SACA are presented for two times, 75 and 125 fm/c, and compared to the ALADIN experimental data [6].

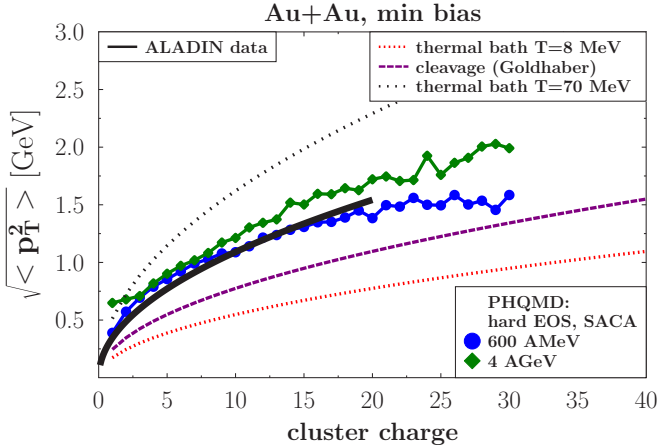


FIG. 27. $\sqrt{\langle p_T^2 \rangle}$ as a function of the cluster charge Z for minimal bias Au + Au collisions at 600A MeV and 4A GeV. The black solid line is an interpolation of the experimental data [6], the blue line with dots and green line with diamonds are the results of PHQMD calculations. The red short-dotted line (black dotted line) represents the result of the thermal model for $T = 8$ (70) MeV. The blue dashed line is the result of the cleavage model of Goldhaber (see text).

extensively analyzed 600A MeV data), there are no measurements of heavy clusters, only of light midrapidity clusters.

Another observable, measured by the ALADIN Collaboration [6], is the rms of the transverse momentum distribution, $\sqrt{\langle p_T^2(Z) \rangle}$, as a function of the cluster charge. In Fig. 27 we show these data in terms of an interpolation line provided by the ALADIN Collaboration [6]. Additionally to the PHQMD results for the 600A MeV and 4A GeV, we also show the expectations from three different theoretical models: a thermal model for temperatures of 8 and 70 MeV and the “cleavage” model of Goldhaber [105]. All three models predict that $\sqrt{\langle p_T^2(Z) \rangle} \propto \sqrt{Z}$. The dotted lines are the expected rms momenta if the clusters are in thermal equilibrium with heat baths of temperature $T = 8$ MeV and $T = 70$ MeV, respectively. Since the binding energy per nucleon of a cluster is around 8 MeV, a temperature considerably higher than 8 MeV would not allow for the existence of clusters. We see that the experimental rms momenta are higher than expected for a heat bath of $T = 8$ MeV, indicated as the red short dotted line in Fig. 27. This questions the assumption that clusters are emitted by a thermal source, as assumed in statistical models.

On the other hand, the apparent inverse slope of the transverse energy spectra of protons at midrapidity for Au + Au at 600A MeV is about 100 MeV. It is a superposition of a thermal contribution and the contribution from the radial flow. 70 MeV is a reasonable value for the thermal part. If clusters are formed from the nucleons of the expanding fireball at the end of the expansion by momentum space coalescence, one would expect that the rms of the transverse momenta distribution of the clusters is of the same order as the black dotted line. Since this scenario is substantially overestimating the experimental data, one would conclude that the late clusterization by coalescence is also not supported by the ALADIN data, not even for light clusters.

The dashed line shows the result expected from the “cleavage” model of Goldhaber, which assumes that the spectator matter is cleaved instantaneously into clusters by penetrating participant nucleons, and that the rms momenta of the clusters are reminiscent of the Fermi motion of the nucleons [105–107]. The difference compared to the prediction of the Goldhaber model comes mainly from the Coulomb repulsion among the clusters and protons, which is not taken into account in the Goldhaber model. The PHQMD calculations agree with data and show the same $\sqrt{\langle p_T^2(Z) \rangle} \propto \sqrt{Z}$ dependence as the data.

C. Hyperclusters

The production of hypernuclei in heavy-ion collisions is one of the challenging experimental and theoretical topics nowadays. Hyperons (Λ 's and Σ 's) are produced in heavy-ion collisions already at SIS energies above 1.6A GeV (which corresponds to the NN threshold). For details of the strangeness production at low energy we refer the reader to the review [46]. In heavy-ion collisions at lower energies the hyperons are almost exclusively produced in the overlapping fireball; however, they may penetrate into the spectator matter and form hyperclusters with spectator nucleons or, during the expansion of the fireball, may find other nucleons with which they form light hyperclusters at midrapidity. Thus, hyperclusters in the projectile/target rapidity regime give information on how these hyperons penetrate the fast moving spectator matter and get accelerated in order to form clusters with spectator nucleons. Hypernuclei around midrapidity are sensitive to the time evolution of the high density zone in the center of the reaction where the hyperons are produced. The study of hyperclusters is one of the research priorities of the upcoming NICA facility and for the Compressed Baryonic Matter (CBM) experiment at FAIR. Statistical model calculations [24] predict that hyperclusters are produced copiously in the energy regime accessible with these facilities.

In this section we extended our study on cluster formation within the PHQMD to hyperclusters, using the MST and SACA cluster finding algorithms. When calculating the hypernuclei with the SACA algorithm, we assume that the strength of the hyperon-nucleon potential is 2/3 of that of nucleon-nucleon potential. We note that the PHQMD describes the hyperon production rather well, as demonstrated in Sec. IV for AGS, SPS, and RHIC energies. This gives us a solid basis to study the hypercluster production within PHQMD.

Figure 28 shows the distribution of $Z = 1$, $Z = 2$ particles, heavier clusters ($Z > 2$), all Λ 's (bound or unbound), as well as of light ($A \leq 4$) and heavy ($A > 4$) hypernuclei identified by the MST algorithm as a function of the rapidity for Au + Au collisions at 4A GeV (upper plot) and at 10A GeV (lower plot). We see an enhancement of the yields of $Z = 1$ particles, Λ 's, and heavier clusters close to projectile and target rapidity and an almost constant distribution for $Z = 1$ particles in between. The production of hyperons increases towards midrapidity. We note that in these calculations we did not make a selection of clusters according to the realistic isospin contents. At midrapidity only a small fraction of the hyperons end up in light hypernuclei, in contradistinction to

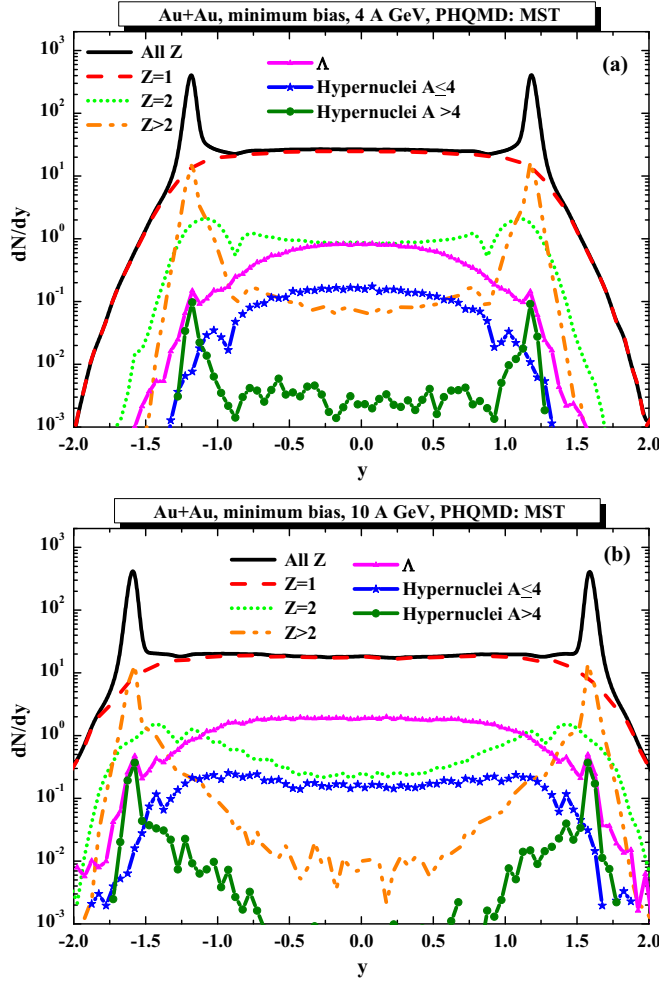


FIG. 28. The PHQMD results (with a hard EoS and the MST algorithm) for the rapidity distributions of all charges (black solid line), $Z = 1$ particles (red dashed line), $Z = 2$ clusters (green dotted line), $Z > 2$ (orange dot-dot-dashed line), all (bound and unbound) Λ 's (magenta line with triangles) as well as light hypernuclei with $A \leq 4$ (blue line with stars) and heavy hypernuclei with $A > 4$ (green line with dots) as a function of the rapidity for central Au + Au collisions at 4A GeV [upper plot (a)] and at 10A GeV [lower plot (b)].

the projectile/target rapidities where many of the produced hyperons end up as part of a larger hypercluster.

In Fig. 29 we show the multiplicity of light and heavy hyperclusters as a function of the impact parameter for Au + Au collisions at 4A GeV. As seen from this figure, the yield of light hyperclusters decreases with the impact parameter, mainly because the overlap region between projectile and target gets smaller and hence fewer hyperons are produced. In central collisions mainly light hypernuclei ($A \leq 4$) are formed, while mid-central collisions are better suited for a study of heavier hypernuclei ($A \geq 5$). Hypernuclei with $A \geq 5$ are dominantly produced by hyperons which enter the spectator matter and get caught there. Therefore, for heavy hypernuclei production there is a competition between the hyperon production which decreases with impact parameter

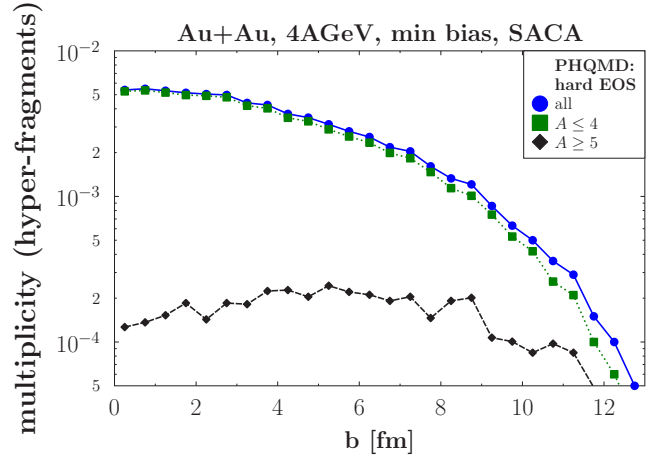


FIG. 29. The multiplicity of light hyperclusters as a function of the impact parameter for Au + Au collisions at 4A GeV calculated with the PHQMD using the SACA cluster recognition algorithm. The blue dots show the multiplicity of all hypernuclei, while the green squares and black rhombi stand for $A \leq 4$ and $A \geq 5$, respectively.

and the spectator matter whose size increases with impact parameter.

VI. CONCLUSION

We have presented a novel microscopic transport approach, PHQMD, to study the dynamics of heavy-ion collisions and cluster and hypernuclei formation at beam energies from a couple of hundred A MeV to ultrarelativistic energies. The PHQMD approach extends, on the one side, the study of cluster formation within the QMD model at lower beam energies and, on the other side, the particle production from SIS to LHC energies within the PHSD approach. The PHQMD adopts the hadronic and partonic collisional interactions from the PHSD approach via the same collision integral. However, it extends the PHSD approach by replacing the mean-field dynamics for the baryon propagation by an n -body quantum molecular dynamics based on density dependent two-body interactions between all baryons in the system. This allows propagation of all baryonic correlations and fluctuations, which is necessary to study the dynamical cluster formation in heavy-ion reactions. This implies that clusters are produced dynamically during the whole heavy-ion collision by the same potential interaction among nucleons which drives their interaction during the heavy-ion collision. Consequently, there is no need to switch to other assumptions for modeling the cluster formation, as done in some other transport approaches by introducing, for example, a coalescence model or a statistical fragmentation model.

For the cluster finding we use the MST and SACA algorithms. The MST finds clusters based on spacial correlations at the end of the reaction while the SACA algorithm, which is based on finding of the most bound configuration, allows us to identify clusters during the early heavy-ion dynamics when clusters still overlap in coordinate space. Moreover, the availability of the mean-field and QMD propagation in one numerical code PHQMD allows us to explore the differences

in the dynamical description of HICs and their influences on cluster formation.

First of all, we have validated the PHQMD approach by comparing the “bulk” hadronic observables as rapidity distributions and m_T or p_T spectra of baryons (p , \bar{p} , Λ , $\bar{\Lambda}$) and mesons (π^\pm , K^\pm) from low SIS to top RHIC energies. We find a reasonably good agreement between the PHQMD results and experimental data. For the QMD dynamics we explore two EoS: “hard” and “soft,” realized by static potentials. We find that

- (i) For the protons the PHQMD results with a soft EoS agree very well with PHSD results. The QMD with a hard EoS shows slightly harder spectra of protons at AGS energies which is favored by experimental data. However, we give a note of caution that in order to draw robust conclusions about the softening or hardening of the EoS one needs to include the momentum dependence of the nuclear potential. This work is under way.
- (ii) For the newly produced hadrons the sensitivity to the EoS is minor in the QMD dynamics. At relativistic energies and at midrapidity the dynamics is driven by hadronic/partonic collisions. The results are thus less sensitive to the baryonic potentials during propagation, and, consequently, the PHSD and PHQMD results are similar. Secondly, within the PHQMD approach we have studied the cluster (including hypernuclei) productions which are identified with the MST and SACA models.
- (iii) We have demonstrated that the QMD dynamics allows formation of clusters at midrapidity as well as at target/projectile rapidity and keeps them stable over time. When using the mean-field propagation, the clusters are not stable and disintegrate with time. This demonstrates the importance of nucleon correlations for the cluster dynamics, which are smeared out in the mean-field propagation.
- (iv) We have validated the PHQMD approach by reproducing the complex cluster pattern observed by the ALADIN Collaboration at the highest energies where experimental data for heavy clusters are available (i.e., beam energies of $600A-1000A$ MeV). We observed that these heavy clusters are produced close to target and projectile rapidity, and with increasing energies also hyper-clusters can be formed in this kinematic region. We find a good description of the ALADIN data for the “rise and fall” of the multiplicity of intermediate mass clusters, $3 \leq Z \leq 30$, emitted in the forward direction as a function of the sum of all forward emitted bound charges, $Z_{\text{bound}2}$. Moreover, the PHQMD calculations with the SACA algorithm show a stability of the clusters versus time. We compared also Z_{max} versus $Z_{\text{bound}2}$ as well as $\sqrt{\langle p_T^2(Z) \rangle}$ as a function of the cluster charge. The latter agrees well with the prediction of an instantaneous breakup of the nucleus and disagrees with the

assumptions that clusters are created in a thermal heat bath with a temperature around the binding energy.

- (v) We have studied also the light cluster production at midrapidity within the PHQMD approach. The identification of light clusters is important for the understanding of the proton spectra at low energies. As has been found by the FOPI Collaboration, in central Au + Au reactions at 1.5A GeV around 40% of all nucleons are bound in clusters. The PHQMD calculations show a good agreement with the FOPI proton data only when subtracting the protons which are bound in clusters. With increasing beam energy up to relativistic energies, the fraction of nucleons bound in clusters decreases however, at beam energies below 5A GeV the identification of clusters is an important issue also for proton observables [9]. We also reproduce the rapidity distribution of light clusters observed at AGS energies, for central as well as for minimum bias data.
- (vi) We made predictions for the production of clusters and hypernuclei at higher beam energies (4A–10A GeV) relevant for the FAIR and NICA experiments. In particular, we presented the rapidity distribution and centrality dependence of hypernuclei production. We investigated also the collective flow of clusters in terms of the v_1 coefficient.

We note that the microscopic origin of the cluster and hypernucleus formation at midrapidity at relativistic energies is one of the intriguing problems of present heavy-ion physics. The measured hadronic transverse energy spectra at midrapidity show an inverse slope parameter in between 100 and 150 MeV, to a large part due to thermal movement of the particles, even if the radial flow contributes as well. Additionally a thermal model fit of the particle ratios at RHIC and LHC energies yields a temperature of the same order. On the other hand clusters are weakly bound objects (with a binding energy of a couple of A MeV) and have a large distance between the cluster nucleons. Consequently, they are not stable in an environment of a temperature of around 100 MeV and collisions with other hadrons can easily destroy them. One may talk about pieces of “ice in a fire.” Therefore it is not evident how these clusters are created and survive the expansion of the system. In this respect the PHQMD approach provides the basis of a more detailed study of their origin since it is based on a microscopic description of the interaction and can be applied early during the collision. The MST method applied in this study for the identification of midrapidity clusters at high energies can identify clusters only at the end of the expansion and is presently “charge blind.” To study the cluster formation process in more detail we have to develop further the SACA approach into a method which can deal with strange baryons and with the quantum features which determine the binding energy of light clusters. Such a development is also necessary to study quantitatively the production of hypernuclei which PHQMD produces copiously. First steps in this direction are under way [56,61].

ACKNOWLEDGMENTS

The authors acknowledge inspiring discussions with C. Blume, W. Cassing, C. Hartnack, P. Moreau, L. Oliva, T. Song, O. Soloveva, Io. Vassiliev, and M. Winn. Furthermore, we acknowledge support by the Deutsche Forschungsgemeinschaft (DFG, German Research Foundation) under Grant No. BR 4000/7-1, by the Russian Science Foundation under Grant No. 19-42-04101, and by the GSI-IN2P3 agreement under Contract No. 13-70. Also we thank the COST Action THOR, CA15213. This project has also received funding from the European Union's Horizon 2020 research and innovation program under Grant Agreement No. 824093. The computational resources were provided by the LOEWE-Center for Scientific Computing and the "Green Cube" at GSI.

APPENDIX A: DYNAMICAL QUASIPARTICLE MODEL (DQPM)

The dynamical quasiparticle model (DQPM) was introduced in Refs. [70,71,108] for the effective description of the properties of the QGP in terms of strongly interacting quarks and gluons, with properties and interactions which are adjusted to reproduce IQCD results on the thermodynamics of the equilibrated QGP at finite temperature T and baryon (or quark) chemical potential μ_q . In the DQPM the quasiparticles are characterized by single-particle Green's functions (in propagator representation) with complex self-energies. The real part of the self-energies is related to the mean-field properties, whereas the imaginary part provides information about the lifetime and/or reaction rates of the particles. This is described by a Lorentzian spectral function [53] of quasiparticles,

$$\rho_j(\omega, \mathbf{p}) = \frac{\gamma_j}{\tilde{E}_j} \left(\frac{1}{(\omega - \tilde{E}_j)^2 + \gamma_j^2} - \frac{1}{(\omega + \tilde{E}_j)^2 + \gamma_j^2} \right) \equiv \frac{4\omega\gamma_j}{(\omega^2 - \mathbf{p}^2 - M_j^2)^2 + 4\gamma_j^2\omega^2} \quad (\text{A1})$$

separately for quarks, antiquarks, and gluons ($j = q, \bar{q}, g$). Here, $\tilde{E}_j^2(\mathbf{p}) = \mathbf{p}^2 + M_j^2 - \gamma_j^2$; the widths γ_j and the masses M_j from the DQPM are functions of the temperature T and the chemical potential μ_q .

Since the DQPM is an effective model, one has to assume the actual form of the (T, μ_q) dependences of the dynamical masses and widths of quasiparticles as well as the coupling. By fixing the quasiparticle properties, one can evaluate the entropy density $s(T, \mu_B)$ and number density in the propagator representation from Baym [109,110] and then, by comparison to the corresponding IQCD data, one can fix the few parameters of the DQPM. After that the DQPM provides a consistent description of the QGP thermodynamics [70,71] and has a predictive power, additionally.

The effective masses are assumed to be given in line with the hard thermal loop (HTL) thermal mass in the asymptotic high-momentum regime, i.e., for gluons by [53]

$$M_g^2(T, \mu_q) = \frac{g^2(T, \mu_q)}{6} \left(\left(N_c + \frac{1}{2} N_f \right) T^2 + \frac{N_c}{2} \sum_q \frac{\mu_q^2}{\pi^2} \right), \quad (\text{A2})$$

and for quarks (antiquarks) by

$$M_{q(\bar{q})}^2(T, \mu_q) = \frac{N_c^2 - 1}{8N_c} g^2(T, \mu_q) \left(T^2 + \frac{\mu_q^2}{\pi^2} \right), \quad (\text{A3})$$

where $N_c = 3$ stands for the number of colors while $N_f (=3)$ denotes the number of flavors. Furthermore, the effective quarks, antiquarks, and gluons in the DQPM have finite widths γ , which are adopted in the form [53]

$$\gamma_g(T, \mu_q) = \frac{1}{3} N_c \frac{g^2(T, \mu_q) T}{8\pi} \ln \left(\frac{2c}{g^2(T, \mu_q)} + 1 \right), \quad (\text{A4})$$

$$\gamma_{q(\bar{q})}(T, \mu_q) = \frac{1}{3} \frac{N_c^2 - 1}{2N_c} \frac{g^2(T, \mu_q) T}{8\pi} \ln \left(\frac{2c}{g^2(T, \mu_q)} + 1 \right), \quad (\text{A5})$$

where $c = 14.4$ is related to a magnetic cutoff, which is a parameter of the DQPM. Furthermore, we assume that the width of the strange quarks is the same as that for the light (u, d) quarks. With the choice of Eq. (A1), the complex self-energies for gluons $\Pi = M_g^2 - 2i\omega\gamma_g$ and for (anti)quarks $\Sigma_q = M_q^2 - 2i\omega\gamma_q$ are fully defined via Eqs. (A2), (A3), (A4), and (A5).

The coupling g^2 , which defines the strength of the interaction in the DQPM, is extracted from IQCD thermodynamics. There are a few realizations of the DQPM for the evaluation of the g^2 : (i) its temperature dependence at vanishing chemical potential can either be obtained by using an ansatz with a few parameters adjusted to results of IQCD thermodynamics [111,112], or (ii) g^2 can directly be obtained by a parametrization of the entropy density from IQCD as in Ref. [113]. We indicate that for the present version of the PHQMD we adopted the DQPM model in the first realization, as used in the PHSD version 4.0 [39,50–53].

The extension of the DQPM to finite baryon chemical potential, μ_B , is performed by using a scaling ansatz which works up to $\mu_B \approx 450$ MeV [114], and which assumes that g^2 is a function of the ratio of the effective temperature $T^* = \sqrt{T^2 + \mu_q^2/\pi^2}$ and the μ_B -dependent critical temperature $T_c(\mu_B)$ as [71]

$$g^2(T/T_c, \mu_B) = g^2 \left(\frac{T^*}{T_c(\mu_B)}, \mu_B = 0 \right) \quad (\text{A6})$$

with $\mu_B = 3\mu_q$ and $T_c(\mu_B) = T_c \sqrt{1 - \alpha \mu_B^2}$, where T_c is the critical temperature at vanishing chemical potential (≈ 0.158 GeV) and $\alpha = 0.974$ GeV⁻². By employing the quasiparticle properties and dressed propagators as given by the DQPM, one can deduce the differential partonic scattering cross sections as well as the interaction rates of light and charm quarks in the QGP as a function of the temperature and the chemical potential [111,113] by calculating the scattering diagrams of the corresponding processes in leading order. This extended version of the DQPM has been employed recently in the PHSD 5.0 [113] and will be adopted by the PHQMD also in future.

APPENDIX B: HADRONIZATION

The hadronization, i.e., the transition from partonic to hadronic degrees of freedom, is described in PHQMD (as well as in PHSD) by local covariant transition rates as introduced in Ref. [39]. For $q + \bar{q}$ fusion to an off-shell meson m of four-momentum $p = (\omega, \mathbf{p})$ at space-time point $x = (t, \mathbf{x})$ it is

$$\begin{aligned} \frac{dN_m(x, p)}{d^4x d^4p} &= \text{Tr}_q \text{Tr}_{\bar{q}} \delta^4(p - p_q - p_{\bar{q}}) \delta^4\left(\frac{x_q + x_{\bar{q}}}{2} - x\right) \\ &\times \omega_q \rho_q(p_q) \omega_{\bar{q}} \rho_{\bar{q}}(p_{\bar{q}}) |v_{q\bar{q}}|^2 \\ &\times W_m(x_q - x_{\bar{q}}, (p_q - p_{\bar{q}})/2) \\ &\times N_q(x_q, p_q) N_{\bar{q}}(x_{\bar{q}}, p_{\bar{q}}) \delta(\text{flavor, color}). \end{aligned} \quad (\text{B1})$$

In Eq. (B1) we introduced the shorthand notation

$$\text{Tr}_j = \sum_j \int d^4x_j \int \frac{d^4p_j}{(2\pi)^4}, \quad (\text{B2})$$

where \sum_j denotes a summation over discrete quantum numbers (spin, flavor, color); $N_j(x, p)$ is the phase-space density of parton j at space-time position x and four-momentum p . In Eq. (B1) $\delta(\text{flavor, color})$ stands symbolically for the conservation of flavor quantum numbers as well as color neutrality of the formed meson m . Furthermore, $v_{q\bar{q}}(\rho_p)$ is the effective quark-antiquark interaction from the DQPM (displayed in Fig. 10 of Ref. [71]) as a function of the local parton ($q +$

$\bar{q} + g$) density ρ_p (or energy density). Furthermore, $W_m(x, p)$ is the dimensionless phase-space distribution of the formed off-shell meson, i.e.,

$$W_m(\xi, p_\xi) = \exp\left(\frac{\xi^2}{2b^2}\right) \exp\left[2b^2(p_\xi^2 - (M_q - M_{\bar{q}})^2/4)\right] \quad (\text{B3})$$

with $\xi = x_1 - x_2 = x_q - x_{\bar{q}}$ and $p_\xi = (p_1 - p_2)/2 = (p_q - p_{\bar{q}})/2$. The width parameter b is fixed by $\sqrt{\langle r^2 \rangle} = b = 0.66$ fm (in the rest frame) which corresponds to an average rms radius of mesons. We note that the expression (B3) corresponds to the limit of independent harmonic oscillator states and that the final hadron-formation rates are approximately independent of the parameter b within reasonable variations. By construction the quantity (B3) is Lorentz invariant; in the limit of instantaneous ‘‘hadron formation,’’ i.e. $\xi^0 = 0$, it provides a Gaussian dropping in the relative distance squared, $(\mathbf{r}_1 - \mathbf{r}_2)^2$. The four-momentum dependence reads explicitly

$$(E_1 - E_2)^2 - (\mathbf{p}_1 - \mathbf{p}_2)^2 - (M_1 - M_2)^2 \leq 0 \quad (\text{B4})$$

and leads to a negative argument of the second exponential in (B3) favoring the fusion of partons with low relative momenta $p_q - p_{\bar{q}} = p_1 - p_2$.

Related transition rates [to Eq. (B1)] have been defined in Ref. [51] also for the fusion of three off-shell quarks ($q_1 + q_2 + q_3 \leftrightarrow B$) to color neutral baryonic (B or \bar{B}) resonances of finite width (or strings) fulfilling energy and momentum conservation as well as flavor current conservation using Jacobi coordinates.

-
- [1] U. Heinz, O. Evdokimov, and P. Jacobs, in *Proceedings of the 26th International Conference on Ultra-relativistic Nucleus-Nucleus Collisions (Quark Matter 2017)* [*Nucl. Phys. A* **967**, vii (2017)].
- [2] S. Borsanyi, Z. Fodor, C. Hoelbling, S. D. Katz, S. Krieg, and K. K. Szabo, *Phys. Lett. B* **730**, 99 (2014).
- [3] A. Bazavov *et al.* (HotQCD Collaboration), *Phys. Rev. D* **90**, 094503 (2014).
- [4] M. Asakawa and K. Yazaki, *Nucl. Phys. A* **504**, 668 (1989).
- [5] M. A. Stephanov, *Prog. Theor. Phys. Suppl.* **153**, 139 (2004).
- [6] A. Schuttauf *et al.*, *Nucl. Phys. A* **607**, 457 (1996).
- [7] C. Sfonti *et al.* (ALADiN2000 Collaboration), *Nucl. Phys. A* **787**, 627 (2007).
- [8] R. Nebauer *et al.* (INDRA Collaboration), *Nucl. Phys. A* **658**, 67 (1999).
- [9] W. Reisdorf *et al.* (FOPI Collaboration), *Nucl. Phys. A* **848**, 366 (2010).
- [10] C. Rappold *et al.* (HypHi Collaboration), *Phys. Lett. B* **747**, 129 (2015).
- [11] T. Anticic *et al.* (NA49 Collaboration), *Phys. Rev. C* **94**, 044906 (2016).
- [12] B. I. Abelev *et al.* (STAR Collaboration), *Science* **328**, 58 (2010).
- [13] H. Agakishiev *et al.* (STAR Collaboration), *Nature (London)* **473**, 353 (2011); **475**, 412(E) (2011).
- [14] J. Adam *et al.* (ALICE Collaboration), *Phys. Lett. B* **754**, 360 (2016).
- [15] J. Adam *et al.* (ALICE Collaboration), *Phys. Rev. C* **93**, 024917 (2016).
- [16] S. Acharya *et al.* (ALICE Collaboration), *Nucl. Phys. A* **971**, 1 (2018).
- [17] E. Shuryak and J. M. Torres-Rincon, *Phys. Rev. C* **100**, 024903 (2019).
- [18] M. Wakai, H. Bando, and M. Sano, *Phys. Rev. C* **38**, 748 (1988).
- [19] Z. Rudy, T. Demski, L. Jarczyk, B. Kamys, P. Kulessa *et al.*, *Z. Phys. A* **351**, 217 (1995).
- [20] T. Gaitanos, H. Lenske, and U. Mosel, *Phys. Lett. B* **675**, 297 (2009).
- [21] V. Topor Pop and S. Das Gupta, *Phys. Rev. C* **81**, 054911 (2010).
- [22] A. S. Botvina, K. K. Gudima, J. Steinheimer, M. Bleicher, and I. N. Mishustin, *Phys. Rev. C* **84**, 064904 (2011); A. S. Botvina, K. K. Gudima, J. Steinheimer, M. Bleicher, and J. Pochodzalla, *ibid.* **95**, 014902 (2017).
- [23] L. Zhu, C. M. Ko, and X. Yin, *Phys. Rev. C* **92**, 064911 (2015).
- [24] A. Andronic, P. Braun-Munzinger, J. Stachel, and H. Stoecker, *Phys. Lett. B* **697**, 203 (2011).
- [25] J. L. Ritman *et al.* (FOPI Collaboration), *Z. Phys. A* **352**, 355 (1995).
- [26] C. David, C. Hartnack, and J. Aichelin, *Nucl. Phys. A* **650**, 358 (1999).
- [27] J. Aichelin, *Phys. Rep.* **202**, 233 (1991).
- [28] J. Aichelin, A. Rosenhauer, G. Peilert, H. Stoecker, and W. Greiner, *Phys. Rev. Lett.* **58**, 1926 (1987).

- [29] J. Aichelin, G. Peilert, A. Bohnet, A. Rosenhauer, H. Stocker, and W. Greiner, *Phys. Rev. C* **37**, 2451 (1988).
- [30] C. Hartnack, R. K. Puri, J. Aichelin, J. Konopka, S. A. Bass, H. Stoecker, and W. Greiner, *Eur. Phys. J. A* **1**, 151 (1998).
- [31] S. A. Bass *et al.*, *Prog. Part. Nucl. Phys.* **41**, 255 (1998).
- [32] M. Bleicher *et al.*, *J. Phys. G* **25**, 1859 (1999).
- [33] H. Kruse, B. V. Jacak, J. J. Molitoris, G. D. Westfall, and H. Stöcker, *Phys. Rev. C* **31**, 1770 (1985).
- [34] J. Aichelin and G. Bertsch, *Phys. Rev. C* **31**, 1730 (1985).
- [35] P. Danielewicz and G. F. Bertsch, *Nucl. Phys. A* **533**, 712 (1991).
- [36] Z. W. Lin, C. M. Ko, B. A. Li, B. Zhang, and S. Pal, *Phys. Rev. C* **72**, 064901 (2005).
- [37] W. Ehehalt and W. Cassing, *Nucl. Phys. A* **602**, 449 (1996).
- [38] W. Cassing and E. L. Bratkovskaya, *Phys. Rep.* **308**, 65 (1999).
- [39] W. Cassing and E. L. Bratkovskaya, *Phys. Rev. C* **78**, 034919 (2008).
- [40] O. Buss *et al.*, *Phys. Rep.* **512**, 1 (2012).
- [41] J. Weil *et al.*, *Phys. Rev. C* **94**, 054905 (2016).
- [42] V. D. Toneev and K. K. Gudima, *Nucl. Phys. A* **400**, 173 (1983); V. D. Toneev, N. S. Amelin, K. K. Gudima, and S. Yu. Sivoklov, *ibid.* **519**, 463 (1990); N. S. Amelin, E. F. Staubo, L. P. Csernai, V. D. Toneev, and K. K. Gudima, *Phys. Rev. C* **44**, 1541 (1991).
- [43] P. B. Gossiaux, D. Keane, S. Wang, and J. Aichelin, *Phys. Rev. C* **51**, 3357 (1995).
- [44] Z. Fecková, J. Steinheimer, B. Tomášik, and M. Bleicher, *Phys. Rev. C* **93**, 054906 (2016).
- [45] A. S. Botvina, J. Steinheimer, E. Bratkovskaya, M. Bleicher, and J. Pochodzalla, *Phys. Lett. B* **742**, 7 (2015).
- [46] C. Hartnack, H. Oeschler, Y. Leifels, E. L. Bratkovskaya, and J. Aichelin, *Phys. Rep.* **510**, 119 (2012).
- [47] D. Oliinychenko, L. G. Pang, H. Elfner, and V. Koch, *Phys. Rev. C* **99**, 044907 (2019).
- [48] R. Marty and J. Aichelin, *Phys. Rev. C* **87**, 034912 (2013).
- [49] R. Marty, E. Bratkovskaya, W. Cassing, and J. Aichelin, *Phys. Rev. C* **92**, 015201 (2015).
- [50] W. Cassing, *Eur. Phys. J.: Spec. Top.* **168**, 3 (2009).
- [51] W. Cassing and E. L. Bratkovskaya, *Nucl. Phys. A* **831**, 215 (2009).
- [52] E. L. Bratkovskaya, W. Cassing, V. P. Konchakovski, and O. Linnyk, *Nucl. Phys. A* **856**, 162 (2011).
- [53] O. Linnyk, E. L. Bratkovskaya, and W. Cassing, *Prog. Part. Nucl. Phys.* **87**, 50 (2016).
- [54] R. K. Puri, C. Hartnack, and J. Aichelin, *Phys. Rev. C* **54**, R28 (1996).
- [55] R. K. Puri and J. Aichelin, *J. Comput. Phys.* **162**, 245 (2000).
- [56] A. Le Fèvre, J. Aichelin, C. Hartnack, and Y. Leifels, *Phys. Rev. C* **100**, 034904 (2019).
- [57] C. Dorso and J. Randrup, *Phys. Lett. B* **301**, 328 (1993).
- [58] A. Le Fèvre *et al.*, *Phys. Rev. C* **80**, 044615 (2009).
- [59] P. B. Gossiaux, R. Puri, C. Hartnack, and J. Aichelin, *Nucl. Phys. A* **619**, 379 (1997).
- [60] A. Le Fèvre and J. Aichelin, *Phys. Rev. Lett.* **100**, 042701 (2008).
- [61] A. Le Fèvre, Y. Leifels, J. Aichelin, C. Hartnack, V. Kireyev, and E. Bratkovskaya, *J. Phys.: Conf. Ser.* **668**, 012021 (2016).
- [62] H. Feldmeier, *Nucl. Phys. A* **515**, 147 (1990).
- [63] L. P. Kadanoff and G. Baym, *Quantum Statistical Mechanics* (Benjamin, New York, 1962).
- [64] S. Juchem, W. Cassing, and C. Greiner, *Nucl. Phys. A* **743**, 92 (2004).
- [65] B. Nilsson-Almqvist and E. Stenlund, *Comput. Phys. Commun.* **43**, 387 (1987); B. Andersson, G. Gustafson, and H. Pi, *Z. Phys. C* **57**, 485 (1993).
- [66] T. Sjostrand, S. Mrenna, and P. Z. Skands, *J. High Energy Phys.* **05** (2006) 026.
- [67] J. Schwinger, *Phys. Rev.* **82**, 664 (1951).
- [68] W. Cassing, A. Palmese, P. Moreau, and E. L. Bratkovskaya, *Phys. Rev. C* **93**, 014902 (2016).
- [69] A. Palmese, W. Cassing, E. Seifert, T. Steinert, P. Moreau, and E. L. Bratkovskaya, *Phys. Rev. C* **94**, 044912 (2016).
- [70] W. Cassing, *Nucl. Phys. A* **791**, 365 (2007).
- [71] W. Cassing, *Nucl. Phys. A* **795**, 70 (2007).
- [72] Y. Aoki, S. Borsanyi, S. Durr, Z. Fodor, S. D. Katz, S. Krieg, and K. K. Szabo, *J. High Energy Phys.* **06** (2009) 088.
- [73] M. Cheng *et al.*, *Phys. Rev. D* **77**, 014511 (2008).
- [74] S. Borsanyi *et al.*, *Phys. Rev. D* **92**, 014505 (2015).
- [75] V. Ozvenchuk, O. Linnyk, M. I. Gorenstein, E. L. Bratkovskaya, and W. Cassing, *Phys. Rev. C* **87**, 024901 (2013).
- [76] W. Cassing, *Nucl. Phys. A* **700**, 618 (2002).
- [77] E. Seifert and W. Cassing, *Phys. Rev. C* **97**, 024913 (2018); **97**, 044907 (2018).
- [78] E. L. Bratkovskaya and W. Cassing, *Nucl. Phys. A* **807**, 214 (2008).
- [79] W. Cassing, L. Tolós, E. L. Bratkovskaya, and A. Ramos, *Nucl. Phys. A* **727**, 59 (2003).
- [80] A. Iñer, D. Cabrera, C. Markert, and E. Bratkovskaya, *Phys. Rev. C* **95**, 014903 (2017); A. Iñer, J. Blair, D. Cabrera, C. Markert, and E. Bratkovskaya, *ibid.* **99**, 024914 (2019).
- [81] A. Ono, H. Horiuchi, T. Maruyama, and A. Ohnishi, *Prog. Theor. Phys.* **87**, 1185 (1992).
- [82] V. P. Konchakovski, E. L. Bratkovskaya, W. Cassing, V. D. Toneev, S. A. Voloshin, and V. Voronyuk, *Phys. Rev. C* **85**, 044922 (2012).
- [83] K. Zbiri *et al.*, *Phys. Rev. C* **75**, 034612 (2007).
- [84] W. Reisdorf *et al.* (FOPI Collaboration), *Nucl. Phys. A* **876**, 1 (2012).
- [85] B. Holzman *et al.* (E917 Collaboration), *Nucl. Phys. A* **698**, 643 (2002).
- [86] L. Ahle *et al.* (E866 and E917 Collaborations), *Phys. Lett. B* **476**, 1 (2000); **490**, 53 (2000).
- [87] W.-C. Chang (E917 Collaboration), *Advances in Nuclear Dynamics 5*, edited by W. Bauer and G. D. Westfall (Springer, Boston, MA, 1999), pp. 215–222.
- [88] Y. Akiba *et al.* (E866 Collaboration), *Nucl. Phys. A* **610**, 139 (1996).
- [89] L. Ahle *et al.* (E877 Collaboration), *Phys. Rev. C* **57**, R466 (1998); J. Barrette *et al.* (E877 Collaboration), *ibid.* **63**, 014902 (2001).
- [90] S. Ahmad *et al.* (E891 Collaboration), *Phys. Lett. B* **382**, 35 (1996); C. Pinkenburg *et al.* (E866 Collaboration), *Nucl. Phys. A* **698**, 495 (2002).
- [91] S. Albergo *et al.* (E896 Collaboration), *Phys. Rev. Lett.* **88**, 062301 (2002).
- [92] H. Appelshäuser *et al.* (NA49 Collaboration), *Phys. Rev. Lett.* **82**, 2471 (1999); C. Blume *et al.*, *J. Phys. G* **34**, S951 (2007); C. Alt *et al.* (NA49 Collaboration), *Phys. Rev. C* **73**, 044910 (2006).

- [93] V. Friese *et al.* (NA49 Collaboration), *J. Phys. G* **30**, S119 (2004); S. V. Afanasiev *et al.*, *Phys. Rev. C* **66**, 054902 (2002); C. Alt *et al.*, *ibid.* **77**, 024903 (2008).
- [94] A. Mischke *et al.* (NA49 Collaboration), *J. Phys. G* **28**, 1761 (2002); A. Mischke *et al.*, *Nucl. Phys. A* **715**, 453c (2003); C. Alt *et al.*, *Phys. Rev. C* **78**, 034918 (2008).
- [95] L. Adamczyk *et al.* (STAR Collaboration), *Phys. Rev. C* **96**, 044904 (2017).
- [96] I. G. Bearden *et al.* (BRAHMS Collaboration), *Phys. Rev. Lett.* **94**, 162301 (2005).
- [97] I. Arsene *et al.* (BRAHMS Collaboration), *Phys. Rev. C* **72**, 014908 (2005).
- [98] S. S. Adler *et al.* (PHENIX Collaboration), *Phys. Rev. C* **69**, 034909 (2004).
- [99] G. Agakishiev *et al.* (STAR Collaboration), *Phys. Rev. Lett.* **108**, 072301 (2012).
- [100] W. Reisdorf *et al.* (FOPI Collaboration), *Nucl. Phys. A* **781**, 459 (2007).
- [101] N. Saito *et al.* (E886 Collaboration), *Phys. Rev. C* **49**, 3211 (1994).
- [102] M. J. Bennett *et al.* (E878 Collaboration), *Phys. Rev. C* **58**, 1155 (1998).
- [103] J. Cleymans, H. Oeschler, K. Redlich, and S. Wheaton, *Phys. Rev. C* **73**, 034905 (2006).
- [104] A. Le Fèvre, Y. Leifels, J. Aichelin, C. Hartnack, V. Kireyev, and E. Bratkovskaya, *Nuovo Cim. C* **39**, 399 (2017).
- [105] A. S. Goldhaber, *Phys. Lett. B* **53**, 306 (1974).
- [106] J. Aichelin and J. Huefner, *Phys. Lett. B* **136**, 15 (1984).
- [107] J. Aichelin, J. Hufner, and R. Ibarra, *Phys. Rev. C* **30**, 107 (1984).
- [108] A. Peshier and W. Cassing, *Phys. Rev. Lett.* **94**, 172301 (2005).
- [109] B. Vanderheyden and G. Baym, *J. Stat. Phys.* **93**, 843 (1998).
- [110] J. P. Blaizot, E. Iancu, and A. Rebhan, *Phys. Rev. D* **63**, 065003 (2001).
- [111] H. Berrehrah, E. Bratkovskaya, W. Cassing, P. B. Gossiaux, J. Aichelin, and M. Bleicher, *Phys. Rev. C* **89**, 054901 (2014).
- [112] H. Berrehrah, E. Bratkovskaya, W. Cassing, P. B. Gossiaux, and J. Aichelin, *Phys. Rev. C* **91**, 054902 (2015).
- [113] P. Moreau, O. Soloveva, L. Oliva, T. Song, W. Cassing, and E. Bratkovskaya, *Phys. Rev. C* **100**, 014911 (2019).
- [114] T. Steinert and W. Cassing, *J. Phys. Conf. Ser.* **1024**, 012029 (2018).